Journal of Computational Physics 540 (2025) 114275

Contents lists available at ScienceDirect

Journal of Computational Physics

journal homepage: www.elsevier.com/locate/jcp

On the ground states of rotating two-component dipolar Bose–Einstein condensates

Wenlei Li [a], Qinglin Tang [b], Jing Wang [c], Yong Zhang [d], Ruijie Zou [d,*]

[a] School of Mathematics, Jilin University, Changchun, 130012, China
[b] School of Mathematics, Sichuan University, Chengdu, 610064, China
[c] Science Building 806, Minzu University of China, Beijing, 100081, China
[d] Center for Applied Mathematics and KL-AAGDM, Tianjin University, Tianjin, 300072, China

ARTICLE INFO

Keywords:
Ground states
Two-component rotating dipolar Bose–Einstein condensates
The gradient flow with Lagrange multiplier method
Kernel truncation method

ABSTRACT

In this paper, we focus on the ground states of rotating two-component dipolar Bose–Einstein condensates. To begin with, we investigate the existence and uniqueness of the ground states with rigorous proofs. Then, we construct a spectrally accurate and efficient numerical scheme by integrating the gradient flow with Lagrange multiplier (GFLM) method and the optimal Kernel Truncation method (KTM) for Dipole-Dipole Interaction (DDI) evaluation to compute the ground states. Finally, we confirm the spectral accuracy, and extensive numerical results are presented to study the effects of different model parameters on the ground states, including the mass distribution, short-range interaction strength, angular velocity and anisotropic trapping potential.

1. Introduction

First resoundingly realized in dilute alkali gases in 1995 [1], Bose–Einstein condensate (BEC) has triggered a worldwide craze especially in atomic, molecular and optical physics and quantum optics. The study of quantized vortices [2,3] related to the superfluid properties of BEC plays a significant role in contemporary physics, thus the rotating BEC opens up a new research field of quantum many-body systems. Recently, the remarkable achievement of the condensate of ^{52}Cr gases [4] by Pfau team at Stuttgart University in 2004 demonstrated very well for the anisotropic and long-range magnetic/electric dipole-dipole interaction. The dipolar BEC bringing in unique phenomena has aroused enormous interests and has been extensively studied since then [5–7]. Moreover, there is growing enthusiasm in exploring the multi-component BEC system not just single one.

At temperature T much smaller than the critical temperature T_c, the properties of rotating two-component dipolar BECs are well described by the macroscopic complex-valued wave function $\Psi = (\psi_1(\mathbf{x}, t), \psi_2(\mathbf{x}, t))^\top$, whose evolution is governed by the coupled Gross–Pitaevskii equations (CGPEs) with Dipole-Dipole Interaction (DDI) term. The d-dimensional ($d = 2$ or 3) dimensionless CGPEs with DDI term in a unified way read as Bao and Cai [5], Zhao et al. [8]:

$$\mathrm{i}\partial_t \psi_\ell(\mathbf{x}, t) = \left[-\frac{1}{2}\Delta + V_\ell(\mathbf{x}) - \Omega L_z + \sum_{i=1}^{2} \left(\beta_{\ell i} |\psi_i(\mathbf{x}, t)|^2 + \lambda_{\ell i} \varphi_i(\mathbf{x}, t) \right) \right] \psi_\ell(\mathbf{x}, t), \quad t > 0, \tag{1.1}$$

* Corresponding author.
E-mail addresses: lwlei@jlu.edu.cn (W. Li), qinglin_tang@scu.edu.cn (Q. Tang), wjing@muc.edu.cn (J. Wang), Zhang_Yong@tju.edu.cn (Y. Zhang), zouruijie@tju.edu.cn (R. Zou).

https://doi.org/10.1016/j.jcp.2025.114275
Received 16 December 2024; Received in revised form 9 July 2025; Accepted 3 August 2025
Available online 6 August 2025

$$\varphi_\ell(\mathbf{x},t) := (U_{\rm dip} * |\psi_\ell|^2)(\mathbf{x},t) = \int_{\mathbb{R}^d} U_{\rm dip}(\mathbf{x}-\mathbf{y})|\psi_\ell(\mathbf{y},t)|^2 {\rm d}\mathbf{y}, \quad \mathbf{x}\in\mathbb{R}^d, \tag{1.2}$$

$$\psi_\ell(\mathbf{x},0) = \psi_\ell^0(\mathbf{x}), \quad \ell = 1,2, \quad \mathbf{x}\in\mathbb{R}^d, \tag{1.3}$$

where the nonlocal potential φ_ℓ representing the long-range interaction between particles, is defined as the convolution of kernel $U_{\rm dip}(\mathbf{x})$ and the density $\rho_\ell(\mathbf{x},t) := |\psi_l(\mathbf{x},t)|^2$. $\mathbf{x} = (x_1,\ldots,x_d)^\top \in \mathbb{R}^d$ $(d = 2,3)$, $\beta_{\ell i}$ and $\lambda_{\ell i}$ are real constants which describe the strength of short-range and long-range interaction (positive/negative for repulsive/attractive interaction) respectively, and $\beta_{12} = \beta_{21}$, $\lambda_{12} = \lambda_{21}$. $L_z = -{\rm i}(x\partial y - y\partial x) = -{\rm i}\partial_\theta$ is the z-component of the angular momentum and Ω characterizes the angular velocity. $V_\ell(\mathbf{x})$ is the given real-valued external trapping potential determined by the type of system under investigation and one common choice is the harmonic potential, i.e. for $\ell = 1,2$,

$$V_\ell(\mathbf{x}) = \frac{1}{2}\begin{cases} \gamma_{x,\ell}^2 x^2 + \gamma_{y,\ell}^2 y^2, & d = 2, \\ \gamma_{x,\ell}^2 x^2 + \gamma_{y,\ell}^2 y^2 + \gamma_{z,\ell}^2 z^2, & d = 3, \end{cases} \tag{1.4}$$

with dimensionless constant $\gamma_{m,\ell}$ representing the trapping frequency in m-direction $(m = x,y,z)$. The wave functions are fast-decaying and smooth under such confining potential, so are the densities. The DDI kernels in (1.2) are given as below [9,10]

$$U_{\rm dip}(\mathbf{x}) := \begin{cases} -\frac{3}{2}(\partial_{\mathbf{n}_\perp\mathbf{n}_\perp} - n_3^2\nabla_\perp^2)\frac{1}{2\pi|\mathbf{x}|}, & d = 2, \\ \frac{3}{4\pi|\mathbf{x}|^3}(1 - \frac{3(\mathbf{x},\mathbf{n})^2}{|\mathbf{x}|^2}), & d = 3. \end{cases} \tag{1.5}$$

Here, $\mathbf{n} = (n_1,n_2,n_3)^\top$ is an unit vector representing the dipole orientation, $\partial_{\mathbf{n}} = \mathbf{n}\cdot\nabla, \partial_{\mathbf{nn}} = \partial_{\mathbf{n}}(\partial_{\mathbf{n}})$, $\mathbf{n}_\perp = (n_1,n_2)^\top, \nabla_\perp = (\partial_x,\partial_y)^\top$, $\partial_{\mathbf{n}_\perp} = \mathbf{n}_\perp\cdot\nabla_\perp$ and $\partial_{\mathbf{n}_\perp\mathbf{n}_\perp} = \partial_{\mathbf{n}_\perp}(\partial_{\mathbf{n}_\perp})$. For the above time dependent CGPEs in (1.1)–(1.3), there exist two important conserved quantities: *mass* and *energy*. *Mass* (or normalization) of the wave functions is defined as

$$\mathcal{N}(t) := \|\Psi(\mathbf{x},t)\|^2 = \mathcal{N}_1(t) + \mathcal{N}_2(t) \equiv \|\Psi(\mathbf{x},0)\|^2 = 1, \quad t\ge 0, \tag{1.6}$$

with $\mathcal{N}_\ell(t)$ $(\ell = 1,2)$ being the mass of each component

$$\begin{cases} \mathcal{N}_1(t) := \int_{\mathbb{R}^d} |\psi_1(\mathbf{x},t)|^2 {\rm d}\mathbf{x} \equiv \mathcal{N}_1(0) = \alpha, & t\ge 0, \\ \mathcal{N}_2(t) := \int_{\mathbb{R}^d} |\psi_2(\mathbf{x},t)|^2 {\rm d}\mathbf{x} \equiv \mathcal{N}_2(0) = 1-\alpha, & t\ge 0, \end{cases} \tag{1.7}$$

with a given $\alpha\in(0,1)$. The *energy* per particle is

$$\mathcal{E}(\Psi(\mathbf{x},t)) := \int_{\mathbb{R}^d}\left[\sum_{\ell=1}^2 \frac{1}{2}|\nabla\psi_\ell|^2 + V_\ell(\mathbf{x})|\psi_\ell|^2 - \Omega\psi_\ell^* L_z\psi_\ell + \frac{1}{2}\sum_{\ell=1}^2\sum_{i=1}^2(\beta_{\ell i}|\psi_\ell|^2|\psi_i|^2 + \lambda_{\ell i}\varphi_\ell|\psi_i|^2)\right]{\rm d}\mathbf{x} \equiv \mathcal{E}(\Psi(\mathbf{x},0)), \ t\ge 0. \tag{1.8}$$

The ground state is defined as the minimizer of the following nonconvex minimization problem

$$\Phi^g(\mathbf{x}) := (\phi_1^g(\mathbf{x}),\phi_2^g(\mathbf{x})) := \operatorname*{argmin}_{\Phi(\mathbf{x})\in\mathbb{S}_\alpha} \mathcal{E}(\Phi(\mathbf{x})), \tag{1.9}$$

with constraint

$$\mathbb{S}_\alpha := \left\{(\phi_1(\mathbf{x}),\phi_2(\mathbf{x}))\middle| \phi_\ell(\mathbf{x})\in H^1(\mathbb{R}^d)\cap L^4(\mathbb{R}^d)\cap L^2_{V_\ell}(\mathbb{R}^d), \ \|\phi_1(\mathbf{x})\|_2^2 = \alpha, \ \|\phi_2(\mathbf{x})\|_2^2 = 1-\alpha\right\}, \tag{1.10}$$

where $L^2_{V_\ell}(\mathbb{R}^d) := \{\phi_\ell(\mathbf{x})|\int_{\mathbb{R}^d} V_\ell(\mathbf{x})|\phi_\ell(\mathbf{x})|^2{\rm d}\mathbf{x} < \infty\}$ is a weighted L^2 space. The ground state is the stationary state with the lowest energy, and satisfy the following nonlinear eigenvalue problem, also named as the Euler–Lagrange equation associated with the energy functional (1.8) under constraint (1.10),

$$\mu_\ell\phi_\ell(\mathbf{x}) = \left[-\frac{1}{2}\Delta + V_\ell(\mathbf{x}) - \Omega L_z + \sum_{i=1}^2(\beta_{\ell i}|\phi_i|^2 + \lambda_{\ell i}\varphi_i)\right]\phi_\ell(\mathbf{x}), \quad \ell = 1,2, \tag{1.11}$$

where $\phi_\ell(\mathbf{x})$ is a time-independent function, μ_ℓ is the Lagrange multiplier or chemical potential of the ℓth component and it can be written as follows

$$\mu_\ell = \frac{1}{\|\phi_\ell\|_2^2}\int_{\mathbb{R}^d}\left[\frac{1}{2}|\nabla\phi_\ell|^2 + V_\ell|\phi_\ell|^2 - \Omega\phi_\ell^* L_z\phi_\ell + \sum_{i=1}^2\left(\beta_{\ell i}|\phi_i|^2 + \lambda_{\ell i}\varphi_i\right)|\phi_\ell|^2\right]{\rm d}\mathbf{x}. \tag{1.12}$$

There have been abundant mathematical and numerical studies on the ground state of the single-component BEC, which are mainly divided into the non-convex constrained optimization based on Gross–Pitaevskii (GP) energy and eigenvalue solvers based on Euler–Lagrange equation. For the former approach, some popular methods are based on proper discretizations of gradient-type flows and their variants [11–15], some other algorithms are based on minimizing the energy functional directly [16–21]. For the latter approach, we refer to Dion and Cancès [22], Wang et al. [23], Xu et al. [24] and references therein. As for the ground states of two-component BECs without DDI term, we refer the readers to Bao and Cai [5], Wang et al. [23], Huang and Yang [25], Wang [26] for more details.

Nevertheless, so far as we know, there are few analytical and numerical literatures on the ground states of two-component BECs with DDI and rotational term. To compute the ground state numerically, the difficulties lie in the accurate and efficient solver for the ground state and long-range DDI evaluation. The gradient flow with Lagrange multiplier (GFLM) method [14] allows for various flexible discretizations and has been successfully applied to multi-component BECs. While, to compute the long-range dipolar potential with great accuracy and efficiency, great challenges arise due to the kernel singularity, convolution nonlocality and density anisotropy, and we refer to Zhang [27] for more details. In fact, there have been several successful fast and accurate solvers proposed based on the Fourier spectral method in the last decade, including the Nonuniform FFT method (NUFFT) [28], Gaussian-sum method (GauSum) [29], Kernel Truncation method (KTM) [30,31] and Anisotropic Truncated Kernel Method (ATKM) [32] etc. Among them, KTM equipped with optimal zero-padding factor [30] seems to be the simplest one to implement, and gains great popularity in the physics community.

In this paper, we choose to adapt GFLM by integrating the optimal KTM to compute DDI, and we prove that a modified energy of the backward/forward Euler discretization scheme is diminishing. Our algorithm is easy to implement and demonstrates excellent performance in both accuracy and efficiency. Overall, the main objectives are threefold:

1. Prove the existence and uniqueness of the ground states.
2. Propose an efficient and accurate algorithm by integrating GFLM method with the optimal KTM to compute the ground states.
3. Confirm the spectral accuracy and investigate the impacts of model parameters on the ground states, including the mass distribution, short-range interaction strength, angular velocity and anisotropic trapping potential.

The rest of the paper is organized as follows: In Section 2, we give an elaborate discussion on the existence and uniqueness of the ground states of two-component dipolar BECs, including the non-rotating case and rotating case, with rigorous proofs. In Section 3, we adapt the gradient flow with Lagrange multiplier (GFLM) method for computing the ground states using the optimal KTM as DDI solver, which achieves spectral accuracy and can be accelerated by FFT with great efficiency. In Section 4, we confirm the spatial spectral accuracy of our algorithm, and explore the ground state patterns under diverse settings of physical parameters in both 2D and 3D. Finally, some concluding remarks are drawn in Section 5.

2. Existence and uniqueness of the ground states

In this section, we shall analyze the existence and uniqueness of the ground states for both non-rotating and rotating cases in d-dimensional spaces.

2.1. Non-rotating case

For non-rotating case, i.e., $\Omega = 0$, the total energy $\mathcal{E}$ is split into three parts

$$\begin{aligned}\mathcal{E}(\Phi(\mathbf{x})) &= \int_{\mathbb{R}^d}\sum_{\ell=1}^{2}\frac{1}{2}|\nabla\phi_\ell|^2 + V_\ell(\mathbf{x})|\phi_\ell|^2\mathrm{d}\mathbf{x} + \int_{\mathbb{R}^d}\sum_{\ell=1}^{2}\frac{\beta_{\ell\ell}}{2}|\phi_\ell|^4 + \beta_{12}|\phi_1|^2|\phi_2|^2\mathrm{d}\mathbf{x} + \int_{\mathbb{R}^d}\sum_{\ell=1}^{2}\frac{\lambda_{\ell\ell}}{2}\varphi_\ell|\phi_\ell|^2 + \lambda_{12}\varphi_1|\phi_2|^2\mathrm{d}\mathbf{x}\\ &:= \mathcal{E}_1(\Phi) + \mathcal{E}_2(\Phi) + \mathcal{E}_3(\Phi).\end{aligned}$$

We introduce four 2×2 matrices related to the model parameters β_{ij} and λ_{ij} as follows

$$B = (\beta_{ij}), \qquad \Lambda = (\lambda_{ij}), \qquad \text{and} \qquad A = B - \Lambda = (a_{ij}), \quad \breve{A} = B + 2\Lambda = (\breve{a}_{ij}). \tag{2.13}$$

To prove the existence of the ground states in non-rotating case, we first prove that the total energy $\mathcal{E}$ is lower bounded.

Lemma 1. *The energy functional $\mathcal{E} \geq 0$ if one of the following cases holds:*

(H_1) *$d = 2$, $n_3 = 0$ and B, Λ are semi-positive definite;*
(H_2) *$d = 2$, $n_3^2 \geq \frac{1}{2}$ and B is semi-positive definite, Λ is semi-negative definite;*
(H_3) *$d = 3$, A and $\breve{A}$ are both semi-positive definite.*

Proof. It is obvious that $\mathcal{E}_1 \geq 0$. For $d = 2$, since B is semi-positive definite, we have $\mathcal{E}_2 \geq 0$. For case (H_1), applying the Plancherel's formula to $\mathcal{E}_3$, we have

$$\mathcal{E}_3(\Phi(\mathbf{x})) = \frac{3}{8\pi^2}\int_{\mathbb{R}^2}\frac{(n_1\xi_1 + n_2\xi_2)^2}{|\xi|}\left(\sum_{\ell=1}^{2}\frac{\lambda_{\ell\ell}}{2}|\widehat{|\phi_\ell|^2}|^2 + \lambda_{12}\overline{\widehat{|\phi_1|^2}}\widehat{|\phi_2|^2}\right)\mathrm{d}\xi \geq 0. \tag{2.14}$$

For case (H_2), from $|\mathbf{n}_\perp\cdot\xi| \leq |\mathbf{n}_\perp||\xi|$ and $n_1^2 + n_2^2 + n_3^2 = 1$, $n_3^2 \geq \frac{1}{2}$, we have

$$\begin{aligned}\mathcal{E}_3(\Phi(\mathbf{x})) &= \frac{3}{8\pi^2}\int_{\mathbb{R}^2}\frac{(n_1\xi_1 + n_2\xi_2)^2 - n_3^2|\xi|^2}{|\xi|}\left(\sum_{\ell=1}^{2}\frac{\lambda_{\ell\ell}}{2}|\widehat{|\phi_\ell|^2}|^2 + \lambda_{12}\overline{\widehat{|\phi_1|^2}}\widehat{|\phi_2|^2}\right)\mathrm{d}\xi\\ &\geq \frac{3}{8\pi^2}\int_{\mathbb{R}^2}(1-2n_3^2)|\xi|\left(\sum_{\ell=1}^{2}\frac{\lambda_{\ell\ell}}{2}|\widehat{|\phi_\ell|^2}|^2 + \lambda_{12}\overline{\widehat{|\phi_1|^2}}\widehat{|\phi_2|^2}\right)\mathrm{d}\xi \geq 0.\end{aligned} \tag{2.15}$$

To deal with case (H_3), noting that the potential corresponding to $1/(4\pi|\mathbf{x}|)$ satisfies the following Poisson equation

$$-\Delta f_\ell(\mathbf{x},t)=\rho_\ell(\mathbf{x},t),\quad \text{with}\lim_{|\mathbf{x}|\to\infty} f_\ell(\mathbf{x},t)=0, \tag{2.16}$$

applying the Plancherel's formula and integration by parts, we get

$$\mathcal{E}_2(\Phi(\mathbf{x}))=\int_{\mathbb{R}^3}\left[\sum_{\ell=1}^{2}\frac{a_{\ell\ell}}{2}|\Delta f_\ell|^2+a_{12}\Delta f_1\Delta f_2\right]\mathrm{d}\mathbf{x}=\frac{1}{16\pi^3}\int_{\mathbb{R}^3}|\xi|^4\left(\sum_{\ell=1}^{2}a_{\ell\ell}|\widehat{f_\ell}|^2+a_{12}(\overline{\widehat{f_1}}\widehat{f_2}+\overline{\widehat{f_2}}\widehat{f_1})\right)\mathrm{d}\xi,$$

$$\mathcal{E}_3(\Phi(\mathbf{x}))=\int_{\mathbb{R}^3}\left[\sum_{\ell=1}^{2}\frac{3\lambda_{\ell\ell}}{2}|\partial_{\mathbf{n}}\nabla f_\ell|^2+3\lambda_{12}\partial_{\mathbf{n}}\nabla f_1\cdot\partial_{\mathbf{n}}\nabla f_2\right]\mathrm{d}\mathbf{x}.$$

Since A is semi-positive definite and $|\mathbf{n}\cdot\xi|\le|\xi|$, we obtain

$$\begin{aligned}\mathcal{E}_2(\Phi(\mathbf{x}))+\mathcal{E}_3(\Phi(\mathbf{x}))&\ge\frac{1}{16\pi^3}\int_{\mathbb{R}^3}|\mathbf{n}\cdot\xi|^2|\xi|^2\left(\sum_{\ell=1}^{2}a_{\ell\ell}|\widehat{f_\ell}|^2+a_{12}(\overline{\widehat{f_1}}\widehat{f_2}+\overline{\widehat{f_2}}\widehat{f_1})\right)\mathrm{d}\xi\\&\quad+\int_{\mathbb{R}^3}\left[\sum_{\ell=1}^{2}\frac{3\lambda_{\ell\ell}}{2}|\partial_{\mathbf{n}}\nabla f_\ell|^2+3\lambda_{12}\partial_{\mathbf{n}}\nabla f_1\cdot\partial_{\mathbf{n}}\nabla f_2\right]\mathrm{d}\mathbf{x}=\int_{\mathbb{R}^3}\left[\sum_{\ell=1}^{2}\frac{\check{a}_{\ell\ell}}{2}|\partial_{\mathbf{n}}\nabla f_\ell|^2+\check{a}_{12}\partial_{\mathbf{n}}\nabla f_1\cdot\partial_{\mathbf{n}}\nabla f_2\right]\mathrm{d}\mathbf{x}\ge 0.\end{aligned}$$

The last inequality holds because $\check{A}$ is semi-positive definite. □

Lemma 2. *Based on Lemma 1, the energy functional $\mathcal{E}(\sqrt{\rho_1},\sqrt{\rho_2})$ is strictly convex with respect to positive pair (ρ_1,ρ_2), $(\sqrt{\rho_1},\sqrt{\rho_2})\in\mathbb{S}_\alpha$.*

Proof. Using Lemma A.1 in Lieb et al. [33], we get the convexity of $\mathcal{E}_1(\sqrt{\rho_1},\sqrt{\rho_2})$. Let $\Phi_1=(\sqrt{\rho_1},\sqrt{\rho_2})\in\mathbb{S}_\alpha$, and $\Phi_2=(\sqrt{\rho_1'},\sqrt{\rho_2'})\in\mathbb{S}_\alpha$, for any $r\in(0,1)$, it is obvious that

$$\Phi=\left(\sqrt{r\rho_1+(1-r)\rho_1'},\sqrt{r\rho_2+(1-r)\rho_2'}\right)\in\mathbb{S}_\alpha.$$

Then for $\mathcal{E}_2(\Phi)$, we get

$$r\mathcal{E}_2(\Phi_1)+(1-r)\mathcal{E}_2(\Phi_2)-\mathcal{E}_2(\Phi)=r(1-r)\int_{\mathbb{R}^d}\left(\sum_{\ell=1}^{2}\frac{\beta_{\ell\ell}}{2}(\rho_\ell-\rho_\ell')^2+\beta_{12}(\rho_1-\rho_1')(\rho_2-\rho_2')\right)\mathrm{d}\mathbf{x}=r(1-r)\mathcal{E}_2(\rho_1-\rho_1',\rho_2-\rho_2'), \tag{2.17}$$

and similarly for $\mathcal{E}_3(\Phi)$, we have

$$\begin{aligned}r\mathcal{E}_3(\Phi_1)+(1-r)\mathcal{E}_3(\Phi_2)-\mathcal{E}_3(\Phi)&=r(1-r)\int_{\mathbb{R}^d}\left(\sum_{\ell=1}^{2}\frac{\lambda_{\ell\ell}}{2}(U_{\mathrm{dip}}*(\rho_\ell-\rho_\ell'))(\rho_\ell-\rho_\ell')+\lambda_{12}(U_{\mathrm{dip}}*(\rho_1-\rho_1'))(\rho_2-\rho_2')\right)\mathrm{d}\mathbf{x}\\&=r(1-r)\mathcal{E}_3(\rho_1-\rho_1',\rho_2-\rho_2').\end{aligned} \tag{2.18}$$

By similar discussions as shown in Lemma 1, we can prove that $\mathcal{E}(\sqrt{\rho_1},\sqrt{\rho_2})$ is strictly convex in (ρ_1,ρ_2). □

Theorem 1. *Under the same assumption of Lemma 1, the minimizer $(\phi_1(\mathbf{x}),\phi_2(\mathbf{x}))$ is of the form $\phi_\ell(\mathbf{x})=e^{\mathrm{i}\theta_\ell}|\phi_\ell(\mathbf{x})|$, for some constant $\theta_\ell\in\mathbb{R}$.*

Proof. From Lemma 1, there exists a minimizing sequence $\{\Phi^n=(\phi_1^n,\phi_2^n)\}_{n=0}^{\infty}\subset\mathbb{S}_\alpha$ and a constant $C>0$, such that

$$\|\nabla\phi_\ell^n\|_2+\|\phi_\ell^n\|_4+\int_{\mathbb{R}^d}V_\ell(\mathbf{x})|\phi_\ell^n|^2\mathrm{d}\mathbf{x}\le C,\quad n\ge 0,\quad \ell=1,2,$$

which implies Φ^n belongs to a weakly compact set in $H^1\cap L^4\cap L^2_{V_\ell}$, therefore, there exists $\Phi^\infty=(\phi_1^\infty,\phi_2^\infty)$ and a subsequence such that

$$\phi_\ell^n\rightharpoonup\phi_\ell^\infty,\ \text{ in } L^2\cap L^4\cap L^2_{V_\ell},\quad \nabla\phi_\ell^n\rightharpoonup\nabla\phi_\ell^\infty,\ \text{ in } L^2,\quad \ell=1,2. \tag{2.19}$$

By the compactness of $L^2_{V_\ell}\hookrightarrow L^2$, we have $\phi_\ell^n\to\phi_\ell^\infty$ in L^2, showing $\|\phi_1^\infty\|_2^2=\alpha$, $\|\phi_2^\infty\|_2^2=1-\alpha\Rightarrow\Phi^\infty\in\mathbb{S}_\alpha$.

Then in order to show $(\phi_1^\infty,\phi_2^\infty)$ is a minimizer, we only need to prove the weakly lower semi-continuity of the total energy $\mathcal{E}$. For the dipolar term, we introduce two operators K_1 and K_2

$$K_1(\rho_\ell^n):=\frac{3}{2}(n_3^2\nabla_\perp^2-\partial_{\mathbf{n}_\perp\mathbf{n}_\perp})[(-\Delta)^{-\frac{1}{2}}\rho_\ell^n],\quad \ell=1,2,\ d=2, \tag{2.20}$$

$$K_2(\rho_\ell^n):=-\rho_\ell^n-3\partial_{\mathbf{nn}}[(-\Delta)^{-1}\rho_\ell^n],\quad \ell=1,2,\ d=3. \tag{2.21}$$

Because the Sobolev norm and the L^2_V norm are both weakly lower semi-continuous, it is easy to get the weakly lower semi-continuity of $\mathcal{E}_1$. Then it remains to prove the weakly lower semi-continuity of $\mathcal{E}_2$ and $\mathcal{E}_3$.

If $d=2$, because of the $L^2(\mathbb{R}^2)$ convergence and $H^1(\mathbb{R}^2)$ weak convergence, we have $\phi_\ell^n\to\phi_\ell^\infty$ in $L^p(\mathbb{R}^2)$ as $n\to\infty$ for $1\le p<\infty$, thus $\mathcal{E}_2(\phi_1^n,\phi_2^n)$ converges to its limit. We know that ρ_ℓ^n belongs to $W^{1,p}(\mathbb{R}^2)$ for some $1<p<2$, and $K_1(\rho_\ell^n)\to K_1(\rho_\ell^\infty)$ in $W^{-1,p'}(\mathbb{R}^2)$, as shown in Lemma 3.2 in Bao et al. [9], then the lower semi-continuity of $\mathcal{E}_3$ follows.

If $d = 3$, owing to $\phi_\ell^n \to \phi_\ell^\infty$ in $L^p(\mathbb{R}^3)$ for $2 \le p < 6$, $\mathcal{E}_2(\phi_1^n, \phi_2^n)$ converges to its limit. Noting that K_2 is a $L^p(\mathbb{R}^3) \to L^p(\mathbb{R}^3)$ $(1 < p < \infty)$ bounded operator [9], then it is easy to prove the convergence of $\mathcal{E}_3(\phi_1^n, \phi_2^n)$.

Now we prove the uniqueness of the ground state, which is similar to Lemma A.4 in Lieb et al. [33]. By the well-known fact: $\|\nabla f\|_2 \ge \|\nabla |f|\|_2$ for any complex function $f \in H^1$, we have $\mathcal{E}_1(\phi_1, \phi_2) \ge \mathcal{E}_1(|\phi_1|, |\phi_2|) \Rightarrow \mathcal{E}(\phi_1, \phi_2) \ge \mathcal{E}(|\phi_1|, |\phi_2|)$, which implies $(|\phi_1|, |\phi_2|)$ is also a minimizer. According to Lemma 2, $(|\phi_1|, |\phi_2|)$ is unique, and $|\phi_\ell|$ is a solution to $-\frac{1}{2}\Delta|\phi_\ell| + W_\ell|\phi_\ell| = \mu_\ell|\phi_\ell|$ for some potential W_ℓ, which is independent of ϕ_1 and ϕ_2, implying that $|\phi_\ell|$ is a ground state. Therefore, the minimizer $(\phi_1(\mathbf{x}), \phi_2(\mathbf{x}))$ is of the form $\phi_\ell(\mathbf{x}) = e^{\mathrm{i}\theta_\ell}|\phi_\ell(\mathbf{x})|$ for some constant $\theta_\ell \in \mathbb{R}$ [34]. □

Then, we give some conditions under which there are no ground states.

Theorem 2. *The energy functional $\mathcal{E}$ is unbounded below on $\mathbb{S}_\alpha$ if one of the following cases holds:*

(H_1') $d = 2$, $n_3 \neq 0$ *and* Λ *is positive-definite;*
(H_2') $d = 2$, $n_3^2 < \frac{1}{2}$ *and* Λ *is negative-definite;*
(H_3') $d = 3$, $\beta_{11} < 0$, *or* $\beta_{22} < 0$, *or* $\beta_{12} < -\frac{\alpha^2\beta_{11} + (1-\alpha)^2\beta_{22}}{\alpha(1-\alpha)}$;
(H_4') $d = 3$, $a_{11} < 0$, *or* $a_{22} < 0$, *or* $a_{12} < -\frac{\alpha^2 a_{11} + (1-\alpha)^2 a_{22}}{\alpha(1-\alpha)}$;
(H_5') $d = 3$, $\check{a}_{11} < 0$, *or* $\check{a}_{22} < 0$, *or* $\check{a}_{12} < -\frac{\alpha^2\check{a}_{11} + (1-\alpha)^2\check{a}_{22}}{\alpha(1-\alpha)}$.

Proof. Similar to Bao et al. [9], we only prove the case $d = 3$ and omit the proof of $d = 2$ for brevity. Without loss of generality, we assume $\mathbf{n} = (0, 0, 1)^\top$, and let

$$\begin{aligned}
&\phi^{\varepsilon_1,\varepsilon_2}(\mathbf{x}) = (\pi\varepsilon_1)^{-\frac{1}{2}}(\pi\varepsilon_2)^{-\frac{1}{4}} e^{-\frac{x^2+y^2}{2\varepsilon_1} - \frac{z^2}{2\varepsilon_2}},\\
&\Phi^{\varepsilon_1,\varepsilon_2}(\mathbf{x}) = (\phi_1^{\varepsilon_1,\varepsilon_2}(\mathbf{x}), \phi_2^{\varepsilon_1,\varepsilon_2}(\mathbf{x})) = (\sqrt{\alpha}\phi^{\varepsilon_1,\varepsilon_2}(\mathbf{x}), \sqrt{1-\alpha}\phi^{\varepsilon_1,\varepsilon_2}(\mathbf{x})),\\
&\Phi_1^{\varepsilon_1,\varepsilon_2}(\mathbf{x}) = (\phi_1^{\varepsilon_1,\varepsilon_2}(\mathbf{x}), \phi_2^{1,1}(\mathbf{x})),\\
&\Phi_2^{\varepsilon_1,\varepsilon_2}(\mathbf{x}) = (\phi_1^{1,1}(\mathbf{x}), \phi_2^{\varepsilon_1,\varepsilon_2}(\mathbf{x})),
\end{aligned} \tag{2.22}$$

with two positive parameters $\varepsilon_1, \varepsilon_2$. We denote $\alpha_1 = \alpha$, $\alpha_2 = 1 - \alpha$ and define

$$-\Delta f_\ell^{\varepsilon_1,\varepsilon_2}(\mathbf{x}) = |\phi_\ell^{\varepsilon_1,\varepsilon_2}(\mathbf{x})|^2, \quad \lim_{|\mathbf{x}|\to\infty} f_\ell^{\varepsilon_1,\varepsilon_2}(\mathbf{x}) = 0, \quad \mathbf{x} \in \mathbb{R}^3, \quad \ell = 1, 2. \tag{2.23}$$

Then it is easy to find that

$$\begin{aligned}
&||\partial_{\mathbf{n}}\nabla f_\ell^{\varepsilon_1,\varepsilon_2}||_2^2 \to \begin{cases} 0, & \varepsilon_2/\varepsilon_1 \to +\infty, \\ \frac{\alpha_\ell^2}{(2\pi)^3\varepsilon_1\sqrt{\varepsilon_2}} \int_{\mathbb{R}^3} |\widehat{|\phi^{1,1}|^2}|^2 \,\mathrm{d}\xi = \alpha_\ell^2 ||\phi^{\varepsilon_1,\varepsilon_2}||_4^4, & \varepsilon_2/\varepsilon_1 \to 0, \end{cases}\\
&\int_{\mathbb{R}^3} \partial_{\mathbf{n}}\nabla f_1^{\varepsilon_1,\varepsilon_2} \cdot \partial_{\mathbf{n}}\nabla f_2^{\varepsilon_1,\varepsilon_2} \mathrm{d}\mathbf{x} \to \begin{cases} 0, & \varepsilon_2/\varepsilon_1 \to +\infty, \\ \frac{\alpha(1-\alpha)}{(2\pi)^3\varepsilon_1\sqrt{\varepsilon_2}} \int_{\mathbb{R}^3} |\widehat{|\phi^{1,1}|^2}|^2 \,\mathrm{d}\xi = \alpha(1-\alpha)||\phi^{\varepsilon_1,\varepsilon_2}||_4^4, & \varepsilon_2/\varepsilon_1 \to 0, \end{cases}
\end{aligned} \tag{2.24}$$

where $||\partial_{\mathbf{n}}\nabla f_\ell^{\varepsilon_1,\varepsilon_2}||_2^2$ and $\int_{\mathbb{R}^3} \partial_{\mathbf{n}}\nabla f_1^{\varepsilon_1,\varepsilon_2} \cdot \partial_{\mathbf{n}}\nabla f_2^{\varepsilon_1,\varepsilon_2} \mathrm{d}\mathbf{x}$ are continuous with respect to $\varepsilon_2/\varepsilon_1 > 0$. Then combining with the above equations, we can get real monotone decreasing functions $\beta(\tau)$ on $(0, \infty)$, such that

$$\lim_{\tau\to 0} \beta(\tau) = 1, \quad \lim_{\tau\to\infty} \beta(\tau) = 0, \tag{2.25}$$

and

$$||\partial_{\mathbf{n}}\nabla f_\ell^{\varepsilon_1,\varepsilon_2}||_2^2 = \beta(\varepsilon_2/\varepsilon_1)\alpha_\ell^2||\phi^{\varepsilon_1,\varepsilon_2}||_4^4, \quad \ell = 1, 2, \quad \int_{\mathbb{R}^3} \partial_{\mathbf{n}}\nabla f_1^{\varepsilon_1,\varepsilon_2} \cdot \partial_{\mathbf{n}}\nabla f_2^{\varepsilon_1,\varepsilon_2} \mathrm{d}\mathbf{x} = \beta(\varepsilon_2/\varepsilon_1)\alpha(1-\alpha)||\phi^{\varepsilon_1,\varepsilon_2}||_4^4. \tag{2.26}$$

Then we can compute the corresponding energy functional for fixed $\varepsilon_1\sqrt{\varepsilon_2}$ as

$$\begin{aligned}
\mathcal{E}(\Phi^{\varepsilon_1,\varepsilon_2}(\mathbf{x})) &= \frac{C_1}{\varepsilon_1\sqrt{\varepsilon_2}}\left[(a_{11} + 3\beta(\varepsilon_2/\varepsilon_1)\lambda_{11})\alpha^2 + (a_{22} + 3\beta(\varepsilon_2/\varepsilon_1)\lambda_{22})(1-\alpha)^2 + 2(a_{12} + 3\beta(\varepsilon_2/\varepsilon_1)\lambda_{12})\alpha(1-\alpha)\right] + \frac{C_2}{\varepsilon_1} + \frac{C_3}{\varepsilon_2} + O(1),\\
\mathcal{E}(\Phi_1^{\varepsilon_1,\varepsilon_2}(\mathbf{x})) &= \frac{C_1}{\varepsilon_1\sqrt{\varepsilon_2}}\left[(a_{11} + 3\beta(\varepsilon_2/\varepsilon_1)\lambda_{11})\alpha^2\right] + \frac{C_2}{\varepsilon_1} + \frac{C_3}{\varepsilon_2} + O(1),\\
\mathcal{E}(\Phi_2^{\varepsilon_1,\varepsilon_2}(\mathbf{x})) &= \frac{C_1}{\varepsilon_1\sqrt{\varepsilon_2}}\left[(a_{22} + 3\beta(\varepsilon_2/\varepsilon_1)\lambda_{22})(1-\alpha)^2\right] + \frac{C_2}{\varepsilon_1} + \frac{C_3}{\varepsilon_2} + O(1),
\end{aligned}$$

with some positive constant $C_j > 0$ $(j = 1, 2, 3)$ independent of ε_1 and ε_2. Fix $\frac{\varepsilon_2}{\varepsilon_1} = \tau_1 > 0$, such that $\beta(\tau_1) = \frac{1}{3}$, we can get the following results. If $\beta_{11} < 0 \Longrightarrow a_{11} + 3\beta(\varepsilon_2/\varepsilon_1)\lambda_{11} = \beta_{11} < 0$, we can easily obtain that

$$\lim_{\varepsilon_1\sqrt{\varepsilon_2}\to+\infty} \mathcal{E}(\Phi_1^{\varepsilon_1,\varepsilon_2}(\mathbf{x})) = -\infty.$$

If $\beta_{22} < 0 \Longrightarrow a_{22} + 3\beta(\varepsilon_2/\varepsilon_1)\lambda_{22} = \beta_{22} < 0$, we have

$$\lim_{\varepsilon_1\sqrt{\varepsilon_2}\to+\infty} \mathcal{E}(\Phi_2^{\varepsilon_1,\varepsilon_2}(\mathbf{x})) = -\infty.$$

If $\beta_{12} < -\frac{\alpha^2\beta_{11}+(1-\alpha)^2\beta_{22}}{\alpha(1-\alpha)}$, we have

$$(a_{11} + 3\beta(\varepsilon_2/\varepsilon_1)\lambda_{11})\alpha^2 + (a_{22} + 3\beta(\varepsilon_2/\varepsilon_1)\lambda_{22})(1-\alpha)^2 + 2(a_{12} + 3\beta(\varepsilon_2/\varepsilon_1)\lambda_{12})\alpha(1-\alpha) = \alpha^2\beta_{11} + (1-\alpha)^2\beta_{22} + \alpha(1-\alpha)\beta_{12} < 0,$$

which leads to

$$\lim_{\varepsilon_1\sqrt{\varepsilon_2}\to+\infty} \mathcal{E}(\Phi^{\varepsilon_1,\varepsilon_2}(\mathbf{x})) = -\infty.$$

Thus the nonexistence of the ground states follows. □

2.2. Rotating case

In this subsection, we make some investigations on the rotating case, i.e., $\Omega \neq 0$. Using Lemma 3.1 in Bao et al. [35], we can easily obtain a similar result as follows.

Theorem 3. *Suppose that $V_\ell(\mathbf{x})$ is given in (1.4), and $|\Omega| < \min\{\gamma_{x,\ell}, \gamma_{y,\ell}\}$. Then the minimization problem (1.9) has a minimizer $\Phi^g = (\phi_1^g, \phi_2^g)$ under the assumption of Lemma 1.*

Proof. Using Young inequality, we have

$$\begin{aligned}\left|\int_{\mathbb{R}^d} -\Omega\phi^* L_z\phi(\mathbf{x})\mathrm{d}\mathbf{x}\right| &\le \int_{\mathbb{R}^d} \left[|\Omega||x\phi^*||\partial_y\phi| + |\Omega||y\phi^*||\partial_x\phi|\right]\mathrm{d}\mathbf{x}\\ &\le \int_{\mathbb{R}^d} \left[\frac{|\Omega|^2}{2}(x^2+y^2)|\phi|^2 + \frac{1}{2}\left(|\partial_x\phi|^2 + |\partial_y\phi|^2\right)\right]\mathrm{d}\mathbf{x},\end{aligned}$$

and for the energy functional $\mathcal{E}$, we obtain the following inequality

$$\begin{aligned}&\int_{\mathbb{R}^d}\left[\sum_{\ell=1}^2\left(V_\ell(\mathbf{x}) - \frac{|\Omega|^2}{2}(x^2+y^2)\right)|\phi_\ell|^2 + \frac{1}{2}\sum_{\ell=1}^2\sum_{i=1}^2(\beta_{\ell i}|\phi_\ell|^2|\phi_i|^2 + \lambda_{\ell i}\varphi_\ell|\phi_i|^2)\right]\mathrm{d}\mathbf{x} \le \mathcal{E}(\Phi(\mathbf{x}))\\ &\le \int_{\mathbb{R}^d}\left[\sum_{\ell=1}^2\left(|\nabla\phi_\ell|^2 + \left(V_\ell(\mathbf{x}) + \frac{|\Omega|^2}{2}(x^2+y^2)\right)|\phi_\ell|^2\right) + \frac{1}{2}\sum_{\ell=1}^2\sum_{i=1}^2(\beta_{\ell i}|\phi_\ell|^2|\phi_i|^2 + \lambda_{\ell i}\varphi_\ell|\phi_i|^2)\right]\mathrm{d}\mathbf{x}.\end{aligned}$$

Then the proof is similar to the non-rotating case and we omit the details. □

2.3. Special case

At last, we consider the special case, i.e., $\alpha = 0, 1$, in which (1.1) can be reduced to

$$\mathrm{i}\partial_t\psi(\mathbf{x},t) = \Big[-\frac{1}{2}\Delta + V(\mathbf{x}) - \Omega L_z + \beta|\psi|^2 + \lambda U_{\mathrm{dip}} * |\psi|^2\Big]\psi(\mathbf{x},t), \tag{2.27}$$

with $\mathbf{x} \in \mathbb{R}^d, t > 0$. And the ground state is usually defined as a minimizer $\phi^g \in S$ such that

$$\mathcal{E}_g := \mathcal{E}(\phi^g) = \min_{\phi\in S}\mathcal{E}(\phi), \tag{2.28}$$

where $S = \{\phi(\mathbf{x})|\phi \in H^1(\mathbb{R}^d) \cap L^4(\mathbb{R}^d) \cap L_V^2(\mathbb{R}^d), \|\phi\|_2 = 1\}$, $\mathcal{E}$ is the energy functional of (2.27), i.e.,

$$\mathcal{E}(\phi(\mathbf{x})) = \int_{\mathbb{R}^d}\left[\frac{1}{2}|\nabla\phi|^2 + V(\mathbf{x})|\phi|^2 + \frac{\beta}{2}|\phi|^4 + \frac{\lambda}{2}(U_{\mathrm{dip}} * |\phi|^2)|\phi|^2 - \Omega\phi^* L_z\phi\right]\mathrm{d}\mathbf{x}.$$

Remark 2.1. For case $\lambda = 0$, the problem (2.27) can be further reduced to the following rotating BEC problem

$$\mathrm{i}\partial_t\psi(\mathbf{x},t) = \Big[-\frac{1}{2}\Delta + V(\mathbf{x}) - \Omega L_z + \beta|\psi|^2\Big]\psi(\mathbf{x},t), \tag{2.29}$$

which has been considered in Bao et al. [35].

We have the following theorem with the same analysis in Bao et al. [9].

Theorem 4. *If $\alpha = 1$, $|\Omega| < \min\{\gamma_{x,1}, \gamma_{y,1}\}$ (or $\alpha = 0$, $|\Omega| < \min\{\gamma_{x,2}, \gamma_{y,2}\}$), and*

1) $d = 2$, $\lambda = 0$, $\beta \ge 0$;
2) $d = 2$, $\lambda > 0$, $\beta \ge 0$, and $n_3 = 0$;
3) $d = 2$, $\lambda < 0$, $\beta \ge 0$, and $n_3^2 \ge \frac{1}{2}$;
4) $d = 3$, $-\frac{1}{2}\beta \le \lambda \le \beta$ with $\beta \ge 0$.

Then there exists a minimizer $\phi^g \in S$ for the minimization problem (2.27) if one of the above conditions holds. Further, (2.27) does not have any minimizer if one of the following cases holds.

1) $d = 2$, $\lambda = 0$, and $\beta < 0$;
2) $d = 2$, $\lambda > 0$, and $n_3 \neq 0$;
3) $d = 2$, $\lambda < 0$, and $n_3^2 < \frac{1}{2}$;
4) $d = 3$, $\beta < 0$, or $\beta \geq 0$ and $\lambda \in (-\infty, -\frac{1}{2}\beta) \cup (\beta, \infty)$.

3. Numerical algorithm

Due to the presence of confining potential, the wave functions decay exponentially fast at the far field, therefore, it is reasonable to truncate the whole space into a rectangular bounded domain, i.e., $\mathbf{R}_L = [-L, L]^d \subset \mathbb{R}^d$, and impose periodic boundary conditions. In this section, we shall first introduce the optimal kernel truncation method to compute the DDI potential, then extend GFLM to the two-component rotating dipolar system.

3.1. Optimal kernel truncation method

To begin with, we can reformulate the dipole potential as follows [36]

$$\varphi(\mathbf{x}) = \begin{cases} \left(\frac{1}{2\pi|\mathbf{x}|}\right) * [-\frac{3}{2}(\partial_{\mathbf{n}_\perp\mathbf{n}_\perp} - n_3^2\nabla_\perp^2)\rho] := \left(\frac{1}{2\pi|\mathbf{x}|} * \widetilde{\rho}\right)(\mathbf{x}), & d = 2, \\ -\rho(\mathbf{x}) - \left(\frac{1}{4\pi|\mathbf{x}|}\right) * (3\partial_{\mathbf{nn}}\rho) := -\rho(\mathbf{x}) - \left(\frac{1}{4\pi|\mathbf{x}|} * \widetilde{\rho}\right)(\mathbf{x}), & d = 3, \end{cases} \tag{3.1}$$

where $\widetilde{\rho} = [-\frac{3}{2}(\partial_{\mathbf{n}_\perp\mathbf{n}_\perp} - n_3^2\nabla_\perp^2)]\rho$ in 2D and $\widetilde{\rho} = 3\partial_{\mathbf{nn}}\rho$ in 3D. In practice, the modified density $\widetilde{\rho}$ can be computed by taking derivatives of Fourier spectral series of ρ on uniform mesh grid with FFT achieving nearly optimal efficiency [29,32]. For presentation simplicity, we omit $\widetilde{\ }$ with an abuse of notations hereafter in this subsection.

The nonlocal potential can be reformulated as follows

$$\varphi(\mathbf{x}) = \int_{\mathbb{R}^d} U(\mathbf{x}-\mathbf{y})\rho(\mathbf{y})\mathrm{d}\mathbf{y} = \int_{\mathbf{R}_L} U(\mathbf{x}-\mathbf{y})\rho(\mathbf{y})\mathrm{d}\mathbf{y} = \int_{\mathbf{x}+\mathbf{R}_L} U(\mathbf{y})\rho(\mathbf{x}-\mathbf{y})\mathrm{d}\mathbf{y} = \int_{\mathcal{B}_G} U(\mathbf{y})\rho(\mathbf{x}-\mathbf{y})\mathrm{d}\mathbf{y}, \quad \mathbf{x} \in \mathbf{R}_L,$$

where $\mathcal{B}_G$ is a ball centered at the origin with radius $G := \max_{\mathbf{x},\mathbf{y}\in\mathbf{R}_L} |\mathbf{x}-\mathbf{y}| = 2\sqrt{d}L$. To achieve spectral accuracy in φ, we first extend the density ρ to $\mathbf{R}_{SL}$ by zero-padding with optimal factor $S = \lceil\sqrt{d}+1\rceil \in \mathbb{Z}^+$ [30] and discretize $\mathbf{R}_{SL}$ using SN equispaced grid points in each spatial direction. Then, we approximate the density with finite Fourier series within $\mathbf{R}_{SL}$ as follows

$$\rho(\mathbf{x}) \approx \rho_N(\mathbf{x}) := \sum_{\mathbf{k}\in\Lambda_{SN}} \widehat{\rho}_{\mathbf{k}}\, e^{\mathrm{i}\mathbf{k}\cdot\mathbf{x}}, \quad \mathbf{x} \in \mathbf{R}_{SL},$$

where

$$\widehat{\rho}_{\mathbf{k}} = \frac{1}{(SN)^d} \sum_{\mathbf{x}_\mathbf{p}\in\mathcal{T}_{SN}} \rho(\mathbf{x}_\mathbf{p})\, e^{-\mathrm{i}\mathbf{k}\cdot\mathbf{x}_\mathbf{p}}, \quad \mathbf{k} \in \Lambda_{SN},$$

with Λ_{SN} and $\mathcal{T}_{SN}$ being the mesh grids in Fourier space and physical space

$$\Lambda_{SN} := \left\{ (k_1, \ldots, k_d) \middle| k_j = (-SN/2, \ldots, SN/2-1)\, \pi/(SL),\ j = 1, \ldots, d \right\}, \tag{3.2}$$

$$\mathcal{T}_{SN} := \left\{ (x_1, \ldots, x_d) \middle| x_j = (-SN/2, \ldots, SN/2-1)(2L/N),\ j = 1, \ldots, d \right\}. \tag{3.3}$$

Thus, we obtain

$$\begin{aligned} \varphi(\mathbf{x}) &\approx \int_{\mathcal{B}_G} U(\mathbf{y})\rho_N(\mathbf{x}-\mathbf{y})\mathrm{d}\mathbf{y}, \\ &= \sum_{\mathbf{k}\in\Lambda_{SN}} \left(\int_{\mathcal{B}_G} U(\mathbf{y}) e^{-\mathrm{i}\mathbf{k}\cdot\mathbf{y}} \mathrm{d}\mathbf{y} \right) \widehat{\rho}_{\mathbf{k}}\, e^{\mathrm{i}\mathbf{k}\cdot\mathbf{x}}, \\ &:= \sum_{\mathbf{k}\in\Lambda_{SN}} \widehat{U_G}(\mathbf{k})\, \widehat{\rho}_{\mathbf{k}}\, e^{\mathrm{i}\mathbf{k}\cdot\mathbf{x}}, \end{aligned} \tag{3.4}$$

where $\widehat{U_G}(\mathbf{k})$, given below as Fourier transform of the kernel on bounded domain,

$$\widehat{U_G}(\mathbf{k}) := \int_{\mathcal{B}_G} U(\mathbf{y}) e^{-\mathrm{i}\mathbf{k}\cdot\mathbf{y}} \mathrm{d}\mathbf{y}, \tag{3.5}$$

usually admits analytical expressions. The numerical solution achieves spectral accuracy, and all the discrete Fourier transforms can be accelerated by FFT with great efficiency. Furthermore, the discrete potential can be rewritten as a discrete convolution of a tensor and discrete density, and such discrete convolution can be accelerated by FFT involving merely a doubly-padded discrete density once the tensor is precomputed once for all. For more details, we refer the readers to Liu et al. [30], Vico et al. [31].

Table 1
The accuracy and computation time (in seconds) of GauSum and KTM.

$N = 256^3$	e_∞	$T_{\text{reg}}(s)$	$T_{\text{cor}}(s)$	$T_{\text{tot}}(s)$
GauSum	8.8866E−16	6.91	0.91	7.82
KTM	5.5648E−16	–	–	6.87

Remark 3.1 (Advantages of KTM over NUFFT [28] and GauSum [29])**.** The NonUniform FFT (NUFFT) method achieves spectral accuracy for the first time and has a complexity $\mathcal{O}(N \log N)$ (N is the total number of the grid points) thanks to NUFFT algorithm [37,38] where the prefactor grows with space dimension, leading to unideal efficiency in high-dimensional problems [39]. While, in GauSum method, the authors utilize a Gaussian-sum approximation of the kernel to split the potential into a regular integral (I_{reg}) and a singular correction integral (I_{cor}) [29]. Compared with existing methods, KTM stands out for its simplicity in implementation and has been widely adopted by the physics community. Given that NUFFT method does not perform as efficiently in three dimension, here, we shall only compare GauSum and KTM in the following example.

Example 3.1 (Comparison of GauSum and KTM)**.** We consider the 3D Coulomb potential ($U = 1/(4\pi|\mathbf{x}|)$) generated by a radial symmetric density $\rho(\mathbf{x}) = e^{-|\mathbf{x}|^2}$, the corresponding Poisson potential could be computed analytically as Exl et al. [29]

$$\varphi(\mathbf{x}) = \frac{\sqrt{\pi}}{4|\mathbf{x}|}\,\mathrm{Erf}(|\mathbf{x}|),$$

where the error function is defined as $\mathrm{Erf}(x) = \frac{2}{\sqrt{\pi}}\int_0^x e^{-t^2}\mathrm{d}t$. The numerical errors are measured in relative l^∞ norm as follows

$$e_\infty := \frac{\|\varphi - \varphi^h\|_\infty}{\|\varphi\|_\infty} = \frac{\max_{\mathbf{x}\in\mathcal{T}_N}|\varphi(\mathbf{x}) - \varphi^h(\mathbf{x})|}{\max_{\mathbf{x}\in\mathcal{T}_N}|\varphi(\mathbf{x})|}.$$

The algorithms were implemented in Fortran and run on a 3.00GH Intel(R) Xeon(R) Gold 6248R CPU with a 36 MB cache in Ubuntu GNU/Linux. Table 1 presents the numerical errors and computation time (measured in seconds) for GauSum and KTM on domain $[-8, 8]^3$, where $T_{\text{reg}}, T_{\text{cor}}$ denote the time spent on evaluation of $I_{\text{reg}}, I_{\text{cor}}$ for GauSum and T_{tot} is the total time. Here, we do not take into account the time spent on the calculation of precomputed Fourier coefficients, which is usually done *once for all* on the same mesh grid and is negligibly small compared with that of multiple potential evaluations.

From Table 1, it can be seen that the execution time of KTM is similar to T_{reg} of GauSum, because both implementations utilize a pair of FFT/iFFT on a zero-padded vector of length $(2N)^3$. In addition, the correction integral T_{cor} of GauSum can be implemented with a pair of FFT/iFFT on a vector of length N^3. We can conclude that KTM performs better in terms of efficiency.

3.2. Gradient flow with lagrange multiplier

The gradient flow with discrete normalization (GFDN) [40], also known as the imaginary time evolution method, is very successful in ground state computation and has been widely adapted to various BECs. In this subsection, we extend a variant, that is, the gradient flow with Lagrange multiplier (GFLM) method [14] that is proved to be effective for multiple constraints (for example, the spinor BEC), to compute the ground states of rotating dipolar two-component BECs by integrating the optimal KTM solver.

Choose a time step $\tau = \Delta t > 0$ and denote the time series as $t_n = n\Delta t$, the continuous GFLM from t_n to t_{n+1} reads as follows

$$\frac{\partial}{\partial t}\phi_\ell(\mathbf{x}, t) = \left[\frac{1}{2}\nabla^2 - V_\ell + \Omega L_z - \sum_{i=1}^{2}(\beta_{\ell i}\,|\phi_i|^2 + \lambda_{\ell i}\,\varphi_i)\right]\phi_\ell(\mathbf{x}, t) + \mu_\ell^n\phi_\ell(\mathbf{x}, t_n), \tag{3.6}$$

$$\phi_\ell(\mathbf{x}, t_{n+1}) := \phi_\ell(\mathbf{x}, t_{n+1}^+) = \sigma_\ell^{n+1}\phi_\ell(\mathbf{x}, t_{n+1}^-), \quad \mathbf{x}\in\mathbf{R}_L, \tag{3.7}$$

$$\Phi(\mathbf{x}, t=0) = \Phi^0(\mathbf{x}) = (\phi_1^0(\mathbf{x}), \phi_2^0(\mathbf{x}))^\top, \quad \text{with } \|\phi_1^0(\mathbf{x})\|_2^2 = \alpha, \quad \|\phi_2^0(\mathbf{x})\|_2^2 = 1-\alpha, \tag{3.8}$$

where μ_ℓ^n are the chemical potentials associated with the ℓth component and the projection coefficients σ_ℓ^{n+1} are given explicitly as follows

$$\sigma_1^{n+1} = \sqrt{\alpha}/\|\phi_1(\cdot, t_{n+1}^-)\|_2, \qquad \sigma_2^{n+1} = \sqrt{1-\alpha}/\|\phi_2(\cdot, t_{n+1}^-)\|_2, \tag{3.9}$$

so as to satisfy the normalization constraint (1.10). We use backward/forward Euler scheme to discretize (3.6) and (3.7) as follows

$$\frac{\phi_\ell^* - \phi_\ell^n}{\tau} = \left(\frac{1}{2}\Delta - s_\ell^n\right)\phi_\ell^* + \left(s_\ell^n - V_\ell + \Omega L_z - \sum_{i=1}^{2}(\beta_{\ell i}|\phi_i^n|^2 + \lambda_{\ell i}\varphi_i^n)\right)\phi_\ell^n + \mu_\ell^n\phi_\ell^n, \tag{3.10}$$

$$\phi_1^{n+1} = \sqrt{\alpha}\,\phi_1^*/\|\phi_1^*\|_2, \quad \phi_2^{n+1} = \sqrt{1-\alpha}\,\phi_2^*/\|\phi_2^*\|_2, \tag{3.11}$$

where $\varphi_i^n(\mathbf{x}) = (U_{\text{dip}} * |\phi_i^n|^2)(\mathbf{x})$ and s_ℓ^n is the stabilization parameter to be determined in a similar way as shown in Liu and Cai [14], Bao et al. [41]. Actually, the above equation is a linear system of ϕ_ℓ^* even without the stabilization term and one can apply preconditioned Krylov subspace solver (BiCGStab for example) [17].

Remark 3.2. Even though we are not sure whether the backward/forward Euler discretization of GFLM (3.10) and (3.11) is energy-diminishing [40] for the moment, we manage to derive the following proposition which ensures that GFLM is stable in the sense that the time step τ can be chosen arbitrary.

Proposition 1. *Define a modified energy as*

$$\mathcal{E}_n(\Phi) = \sum_{\ell=1}^{2} \mathcal{E}_{n,\ell}(\phi_\ell) := \sum_{\ell=1}^{2} \int_{\mathbf{R}_L} \left[\frac{1}{2}|\nabla\phi_\ell|^2 + V_\ell|\phi_\ell|^2 - \Omega\phi_\ell^* L_z\phi_\ell + \sum_{i=1}^{2}(\beta_{\ell i}|\phi_i^n|^2 + \lambda_{\ell i}\varphi_i^n)|\phi_\ell|^2 \right] \mathrm{d}\mathbf{x}, \tag{3.12}$$

for $\Phi := (\phi_1, \phi_2)^\top \in \mathbb{S}_\alpha$. *Let* $V_\ell(\mathbf{x}) \in L^\infty(\mathbf{R}_L)$ *and* $\phi_\ell^n \in L^\infty(\mathbf{R}_L)$, *suppose that*

$$s_\ell^n \geq \frac{1}{2}\max\left\{0, \sup_{\mathbf{x}\in\mathbf{R}_L}\left\{V_\ell(\mathbf{x}) + \sum_{i=1}^{2}(\beta_{\ell i}|\phi_i^n|^2 + \lambda_{\ell i}\varphi_i^n) + \frac{\Omega^2}{2}(x^2+y^2) - \mu_\ell^n\right\}\right\},$$

Then, for any $\tau \geq 0$, *the backward/forward Euler discretization* (3.10) *and* (3.11) *satisfies the modified energy dissipation property:*

$$\mathcal{E}_n(\Phi^{n+1}) \leq \mathcal{E}_n(\Phi^n).$$

Proof. Multiply both sides of (3.10) by $\overline{\phi_\ell^* - \phi_\ell^n}$ and integrate them with respect to $\mathbf{x}$ over $\mathbf{R}_L$, we have

$$\begin{aligned}
2\frac{1+s_\ell^n\tau}{\tau}\|\phi_\ell^* - \phi_\ell^n\|_2^2 &= \mathcal{E}_{n,\ell}(\phi_\ell^n) - \mathcal{E}_{n,\ell}(\phi_\ell^*) - \frac{1}{2}\|\nabla(\phi_\ell^* - \phi_\ell^n)\|_2^2 - \mu_\ell^n(\|\phi_\ell^n\|_2^2 - \|\phi_\ell^*\|_2^2) \\
&\quad + \int_{\mathbf{R}_L}\left(V_\ell + \sum_{i=1}^{2}(\beta_{\ell i}|\phi_i^n|^2 + \lambda_{\ell i}\varphi_i^n) - \Omega L_z - \mu_\ell^n\right)|\phi_\ell^* - \phi_\ell^n|^2\mathrm{d}\mathbf{x} \\
&= -\mathcal{E}_{n,\ell}(\phi_\ell^*) - \frac{1}{2}\|\nabla(\phi_\ell^* - \phi_\ell^n)\|_2^2 + \mu_\ell^n\|\phi_\ell^*\|_2^2 \\
&\quad + \int_{\mathbf{R}_L}\left(V_\ell + \sum_{i=1}^{2}(\beta_{\ell i}|\phi_i^n|^2 + \lambda_{\ell i}\varphi_i^n) - \Omega L_z - \mu_\ell^n\right)|\phi_\ell^* - \phi_\ell^n|^2\mathrm{d}\mathbf{x} \leq -\mathcal{E}_{n,\ell}(\phi_\ell^*) + \mu_\ell^n\|\phi_\ell^*\|_2^2 \\
&\quad + \int_{\mathbf{R}_L}\left(V_\ell + \sum_{i=1}^{2}(\beta_{\ell i}|\phi_i^n|^2 + \lambda_{\ell i}\varphi_i^n) + \frac{\Omega^2}{2}(x^2+y^2) - \mu_\ell^n\right)|\phi_\ell^* - \phi_\ell^n|^2\mathrm{d}\mathbf{x} \\
&\leq -\mathcal{E}_{n,\ell}(\phi_\ell^*) + \mu_\ell^n\|\phi_\ell^*\|_2^2 + 2s_\ell^n\|\phi_\ell^* - \phi_\ell^n\|_2^2,
\end{aligned}$$

which immediately implies that

$$\mathcal{E}_{n,1}(\phi_1^{n+1}) \leq \alpha\mu_1^n = \mathcal{E}_{n,1}(\phi_1^n), \qquad \mathcal{E}_{n,2}(\phi_2^{n+1}) \leq (1-\alpha)\mu_2^n = \mathcal{E}_{n,2}(\phi_2^n).$$

Here we abuse the notation of L^2 norm as integral over bounded domain $\mathbf{R}_L$. Then, we can prove that $\mathcal{E}_n(\Phi^{n+1}) = \sum_{\ell=1}^{2}\mathcal{E}_{n,\ell}(\phi_\ell^{n+1}) \leq \sum_{\ell=1}^{2}\mathcal{E}_{n,\ell}(\phi_\ell^n) = \mathcal{E}_n(\Phi^n)$. □

To derive the full discrete scheme, we shall first discuss the spatial discretization. Since the wave functions are smooth and decay fast at the far field, we apply Fourier pseudo-spectral method to approximate the wave functions on uniform mesh grid, achieving spectral accuracy, and more importantly, all the computations related to spatial approximation can be accelerated by discrete Fast Fourier transform (FFT) with optimal efficiency. For simplicity, here we only present details for the 2D case and generalization to 3D is straightforward. The computation domain $\mathbf{R}_L = [-L, L]^2$ is uniformly discretized in each spatial direction with the same mesh size $h_x = h_y = h = (2L)/N$ where $N \in 2\mathbb{Z}^+$ is an even positive integer. The mesh grids in Fourier space and physical space are defined similarly to those in (3.2) and (3.3).

Introduce the Fourier basis functions as

$$W_{\mathbf{k}}(\mathbf{x}) = e^{\mathrm{i}\mathbf{k}\cdot(\mathbf{x}+L)}, \quad \mathbf{k} := (k_x, k_y) \in \Lambda_N.$$

The Fourier pseudo-spectral approximations of the wave function $\phi_\ell, \Delta\phi_\ell, L_z\phi_\ell$ at grid point $\mathbf{x}_\mathbf{p} := (x_i, y_j) \in \mathcal{T}_N$ are given as follows

$$\begin{aligned}
&\phi_\ell(\mathbf{x}_\mathbf{p}) \approx \frac{1}{N^2}\sum_{\mathbf{k}\in\Lambda_N}\widehat{(\phi_\ell)}_\mathbf{k} W_\mathbf{k}(\mathbf{x}_\mathbf{p}), \qquad (\Delta\phi_\ell)(\mathbf{x}_\mathbf{p}) \approx (\llbracket\Delta\rrbracket\phi_\ell)_{ij} := -\frac{1}{N^2}\sum_{\mathbf{k}\in\Lambda_N}|\mathbf{k}|^2\widehat{(\phi_\ell)}_\mathbf{k} W_\mathbf{k}(\mathbf{x}_\mathbf{p}), \\
&(L_z\phi_\ell)(\mathbf{x}_\mathbf{p}) \approx (\llbracket L_z\rrbracket\phi_\ell)_{ij} := \frac{1}{N^2}\sum_{\mathbf{k}\in\Lambda_N}(x_i k_y - y_j k_x)\widehat{(\phi_\ell)}_\mathbf{k}\, W_\mathbf{k}(\mathbf{x}_\mathbf{p}),
\end{aligned}$$

where the Fourier coefficients $\widehat{(\phi_\ell)}_\mathbf{k}$ are defined as

$$\widehat{(\phi_\ell)}_\mathbf{k} := \sum_{\mathbf{x}_\mathbf{p}\in\mathcal{T}_N}\phi_\ell(\mathbf{x}_\mathbf{p})\,\overline{W_\mathbf{k}(\mathbf{x}_\mathbf{p})}, \qquad \mathbf{k} \in \Lambda_N.$$

The numerical approximation of $\phi_\ell(x_i, y_j, t_n), V_\ell(x_i, y_j)$ are denoted by $\phi_{\ell,ij}^n$ and $V_{\ell,ij}$ respectively. Then the full discrete scheme reads as

$$\frac{\phi_{\ell,ij}^* - \phi_{\ell,ij}^n}{\tau} = \left(\frac{1}{2}\llbracket\Delta\rrbracket - s_\ell^n\right)\phi_{\ell,ij}^* + \left(s_\ell^n - V_{\ell,ij} + \Omega\llbracket L_z\rrbracket - \sum_{m=1}^{2}(\beta_{\ell m}|\phi_{m,ij}^n|^2 + \lambda_{\ell m}\varphi_{m,ij}^n) + \mu_\ell^n\right)\phi_{\ell,ij}^n,$$

and the optimal stabilization parameters s_ℓ^n are chosen numerically as $s_\ell^n = \frac{1}{2}(b_{\ell,\max}^n + b_{\ell,\min}^n)$ with

$$b_{\ell,\max}^n = \max_{i,j} G_{\ell,ij}^n, \quad b_{\ell,\min}^n = \min_{i,j} G_{\ell,ij}^n, \quad G_{\ell,ij}^n := V_{\ell,ij} + \sum_{m=1}^{2} (\beta_{\ell m} |\phi_{m,ij}^n|^2 + \lambda_{\ell m} \varphi_{m,ij}^n).$$

The above equation is actually a linear system for ϕ_ℓ^* and can be solved in Fourier space more efficiently. We omit details here for brevity and refer readers to Liu and Cai [14], Bao et al. [41].

4. Numerical results

As shown in the previous section, we combine the GFLM and KTM to compute the ground states, and denote such algorithm as GFLM-KTM. In this section, we shall first confirm the spatial accuracy in both 2D and 3D, then compute the ground states under different parameters, including the mass distribution, short-range interaction strength and angular velocity. In addition, we also study the effect of anisotropic trapping potential on the structure of quantized vortices. Moreover, we investigate the stripe-patterned vortex structures in the two-component system, where one component contains DDI while the other is non-dipolar. Finally, we explore the vortex patterns with different angular velocities in 3D.

Numerically, to compute the ground states, the initial data for each component can be chosen from the following 10 frequently-used types, and the stopping criterion is adopted as follows

$$\|\boldsymbol{\phi}_1^{n+1} - \boldsymbol{\phi}_1^n\|_\infty \le \varepsilon \quad \& \quad \|\boldsymbol{\phi}_2^{n+1} - \boldsymbol{\phi}_2^n\|_\infty \le \varepsilon, \tag{4.13}$$

where $\varepsilon \ll 1$ is the desired tolerance. The resulted one with the lowest energy is then regarded as the ground state:

$$(a)\ \phi_\ell^a(\mathbf{x}) = c_\ell \pi^{-\frac{d}{4}} e^{\frac{-|\mathbf{x}|^2}{2}}, \qquad (b)\ \phi_\ell^b(\mathbf{x}) = c_\ell \frac{(x+\mathrm{i}y)\phi_\ell^a(\mathbf{x})}{\|(x+\mathrm{i}y)\phi_\ell^a(\mathbf{x})\|}, \qquad (\bar{b})\ \phi_\ell^{\bar{b}}(\mathbf{x}) = \overline{\phi_\ell^b(\mathbf{x})},$$

$$(c)\ \phi_\ell^c(\mathbf{x}) = c_\ell \frac{\phi_\ell^a(\mathbf{x}) + \phi_\ell^b(\mathbf{x})}{\|\phi_\ell^a(\mathbf{x}) + \phi_\ell^b(\mathbf{x})\|}, \qquad (\bar{c})\ \phi_\ell^{\bar{c}}(\mathbf{x}) = \overline{\phi_\ell^c(\mathbf{x})}, \qquad (d)\ \phi_\ell^d(\mathbf{x}) = c_\ell \frac{(1-\Omega)\phi_\ell^a(\mathbf{x}) + \Omega\phi_\ell^b(\mathbf{x})}{\|(1-\Omega)\phi_\ell^a(\mathbf{x}) + \Omega\phi_\ell^b(\mathbf{x})\|},$$

$$(\bar{d})\ \phi_\ell^{\bar{d}}(\mathbf{x}) = \overline{\phi_\ell^d(\mathbf{x})}, \qquad (e)\ \phi_\ell^e(\mathbf{x}) = c_\ell \frac{\Omega\phi_\ell^a(\mathbf{x}) + (1-\Omega)\phi_\ell^b(\mathbf{x})}{\|\Omega\phi_\ell^a(\mathbf{x}) + (1-\Omega)\phi_\ell^b(\mathbf{x})\|}, \qquad (\bar{e})\ \phi_\ell^{\bar{e}}(\mathbf{x}) = \overline{\phi_\ell^e(\mathbf{x})},$$

$$(f)\ \phi_\ell^f(\mathbf{x}) = c_\ell \frac{\phi_\ell^{\mathrm{TF}}(\mathbf{x})}{\|\phi_\ell^{\mathrm{TF}}(\mathbf{x})\|},$$

where the last one is the Thomas-Fermi approximation, with

$$\phi_\ell^{\mathrm{TF}}(\mathbf{x}) = \begin{cases} \sqrt{\frac{\mu_\ell^{\mathrm{TF}} - V_\ell(\mathbf{x})}{\max(\beta_{\ell\ell}, \beta_{12})}}, & V_\ell(\mathbf{x}) < \mu_\ell^{\mathrm{TF}}, \\ 0, & \text{otherwise}, \end{cases} \quad \mu_\ell^{\mathrm{TF}} = \frac{1}{2} \begin{cases} (4\max(\beta_{\ell\ell}, \beta_{12})/\pi)^{1/2}, & d = 2, \\ (15\max(\beta_{\ell\ell}, \beta_{12})/4\pi)^{2/5}, & d = 3, \end{cases}$$

and $c_1 = \sqrt{\alpha},\ c_2 = \sqrt{1-\alpha}$.

In the following numerical tests, unless stated otherwise, we choose the computational domain as $\mathbf{R}_L = [-16, 16]^d$, the mesh size in each direction as $h = 1/4$, the time step as $\tau = 0.1$, and the desired tolerance of the stopping criterion as $\varepsilon = 10^{-10}$. We take the same isotropic harmonic trapping potential for each component, i.e., $V_1(\mathbf{x}) = V_2(\mathbf{x}) = |\mathbf{x}|^2/2$, and the dipole orientation $\boldsymbol{n} = (1, 0, 0)^\top$. The algorithm was implemented in Fortran and run on a 3.00 GHz Intel(R) Xeon(R) Gold 6248R CPU with a 36 MB cache in Ubuntu GNU/Linux.

4.1. Accuracy confirmation

For harmonic trapping potential, the energies of the ground state $\Phi^g := (\phi_1^g, \phi_2^g)$ satisfy the following *virial identity*

$$I(\Phi^g) := 2E_{\mathrm{kin}}(\Phi^g) + dE_{\mathrm{int}}(\Phi^g) - 2E_{\mathrm{pot}}(\Phi^g) + 3E_{\mathrm{dip}}(\Phi^g) = 0, \tag{4.1}$$

which is similar as in the single-component non-rotating BEC [5] and can be used as the benchmark to test the accuracy of our algorithm. The kinetic energy $E_{\mathrm{kin}}(\Phi^g)$, interaction energy $E_{\mathrm{int}}(\Phi^g)$, potential energy $E_{\mathrm{pot}}(\Phi^g)$ and dipolar energy $E_{\mathrm{dip}}(\Phi^g)$ are defined

Table 2
Numerical errors of the ground states in both 2D and 3D.

	h	$\lvert\mathcal{E}_g - \mathcal{E}_g^h\rvert$	$\lvert\mu_1 - \mu_1^h\rvert$	$\lvert\mu_2 - \mu_2^h\rvert$	e_1^h	e_2^h	$\lvert I_g^h\rvert$
2D	1	6.1494E−04	5.4000E−03	5.7000E−03	3.6000E−03	6.9000E−03	2.9300E−02
	1/2	6.9304E−07	3.4110E−06	3.5881E−06	4.4668E−05	8.0687E−05	2.8138E−05
	1/4	9.0594E−14	5.6914E−12	5.9934E−12	3.7949E−09	7.3684E−09	1.9971E−11
	1/8	4.6185E−14	1.0836E−13	6.2172E−14	1.6418E−12	5.3128E−13	3.2856E−14
3D	1	7.2126E−04	2.5000E−03	2.5000E−03	8.8000E−03	8.6000E−03	2.0354E−02
	1/2	6.1388E−07	6.3115E−07	6.1437E−07	8.4864E−05	8.3238E−05	1.6160E−05
	1/4	1.3802E−12	3.1499E−12	2.8999E−12	9.0462E−09	8.8609E−09	9.3334E−12
	1/8	1.2603E−12	1.0836E−13	1.3012E−13	2.9803E−12	2.5302E−12	1.1933E−12

as follows

$$E_{\rm kin}(\Phi^g) = \frac{1}{2}\int_{\mathbb{R}^d}\sum_{\ell=1}^{2}|\nabla\phi_\ell^g|^2{\rm d}\mathbf{x}, \qquad E_{\rm int}(\Phi^g) = \frac{1}{2}\int_{\mathbb{R}^d}\sum_{\ell=1}^{2}\sum_{i=1}^{2}\beta_{\ell i}\left|\phi_\ell^g\right|^2\left|\phi_i^g\right|^2{\rm d}\mathbf{x},$$

$$E_{\rm pot}(\Phi^g) = \int_{\mathbb{R}^d}\sum_{\ell=1}^{2}V_\ell(\mathbf{x})|\phi_\ell^g|^2{\rm d}\mathbf{x}, \qquad E_{\rm dip}(\Phi^g) = \frac{1}{2}\int_{\mathbb{R}^d}\sum_{\ell=1}^{2}\sum_{i=1}^{2}\lambda_{\ell i}\,\varphi_\ell^g\,|\phi_i^g|^2{\rm d}\mathbf{x}.$$

For simplicity, we denote I_g^h as the approximation of $I(\Phi^g)$ obtained with mesh size h, $\mu_\ell := \mu_\ell(\Phi^g)$ as the chemical potentials and $\mathcal{E}_g := \mathcal{E}(\Phi^g)$ as the ground state energy. The numerical errors of the ground states are measured in relative maximum norm, i.e.,

$$e_\ell^h := \|\phi_\ell - \phi_\ell^h\|_\infty / \|\phi_\ell\|_\infty = \max_{\mathbf{x}\in\mathcal{T}_N}|\phi_\ell(\mathbf{x}) - \phi_\ell^h(\mathbf{x})| / \max_{\mathbf{x}\in\mathcal{T}_N}|\phi_\ell(\mathbf{x})|, \tag{4.2}$$

where ϕ_ℓ, ϕ_ℓ^h are the benchmark solutions, and numerical wave functions that are obtained with mesh size h respectively.

Example 4.1. In this example, we verify the accuracy of our method in both 2D and 3D. To this end, for 2D case, we fix $\beta_{11} : \beta_{12} : \beta_{22} = 500(1 : 0.94 : 0.97)$, $\Omega = 0.1,\ \alpha = 0.1,\ \lambda_{11} = 1,\ \lambda_{12} = 2,\ \lambda_{22} = 4$, the dipole axis $\boldsymbol{n} = (0, 1, 0)^\top$, and $\varepsilon = 10^{-11}$ in (4.13). In 3D, we choose $\mathbf{R}_L = [-8, 8]^3, \beta_{11} : \beta_{12} : \beta_{22} = 100 : 98 : 99,\ \Omega = 0.1,\ \alpha = 0.5,\ \lambda_{11} = \lambda_{12} = \lambda_{22} = 75,\ \varepsilon = 10^{-10}$ and the dipole axis $\boldsymbol{n} = (0, 0, 1)^\top$.

Table 2 presents the spatial errors in both 2D and 3D, from which we can conclude that GFLM-KTM is spectrally accurate in space. The benchmark solutions are obtained with a very small mesh size $h = 1/16$. In 2D, ground state energy $\mathcal{E}_g = 8.3727$, chemical potentials $\mu_1 = 12.2977$, $\mu_2 = 12.4845$. While in 3D, ground state energy $\mathcal{E}_g = 8.3000$, chemical potentials $\mu_1 = 3.5609$, $\mu_2 = 3.5513$. The numerical chemical potentials and numerical ground state energy are denoted by μ_ℓ^h and $\mathcal{E}_g^h$.

4.2. Effects of different model parameters

In this subsection, we investigate the effects of different model parameters on the structure of ground states for 2D case, focusing on the mass distribution, short-range interaction strength, angular velocity, and anisotropic trapping potential. Unless specified otherwise, in all the figures showed below, the first row represents the density of the first component, while the second row denotes that of the second component.

Example 4.2 (Mass distribution)**.** In this example, we study the ground states under different mass distribution parameters α. To this end, we take $\beta_{11} : \beta_{12} : \beta_{22} = 350(1 : 0.9 : 1),\ \Omega = 0.3,\ \lambda_{11} = \lambda_{12} = \lambda_{22} = 125$.

Fig. 1 shows the contour plots of the density $|\phi_\ell^g|^2$ with varied $\alpha = 0.2,\ 0.3,\ 0.4,\ 0.5$. It is clear to see that: (i) For the component with smaller mass, the distance of two density peaks decreases as α increases. (ii) If the two components have equal mass, the vortex numbers of both components are identical.

Example 4.3 (Short-range interaction strength & angular velocity)**.** Here, we compute the ground states under different ratios of short-range interaction strength parameters β_{11}, β_{12} and β_{22}, and observe the vortex patterns with various angular velocities. In our simulations, we choose $\lambda_{11} = \lambda_{12} = \lambda_{22} = 100,\ \alpha = 0.5$ and different $\Omega = 0.1, 0.15, 0.25, 0.3$. The following two cases are considered

- **Case I :** Fix $\beta_{11} : \beta_{12} : \beta_{22} = 575(1 : 0.96 : 0.97)$, vary $\Omega = 0.1, 0.15, 0.25, 0.3$.
- **Case II :** Fix $\beta_{11} : \beta_{12} : \beta_{22} = 575(1 : 0.95 : 1)$, vary $\Omega = 0.1, 0.15, 0.25, 0.3$.

Figs. 2 and 3 depict the contour plots of the density $|\phi_\ell^g|^2$ under different ratios of β_{11}, β_{12} and β_{22}, and various Ω. From these figures, we can know that: (i) For the component with stronger intra-component short-range interaction, the vortex number increases as angular velocity increases (cf. Fig. 2). (ii) If the two components have the same intra-component short-range interaction strength, the vortex numbers of both components are identical when $\Omega = 0.25$ and 0.3 (cf. Fig. 3). (iii) The total number of vortices in the two-component system increases as angular velocity rises (cf. Figs. 2 and 3).

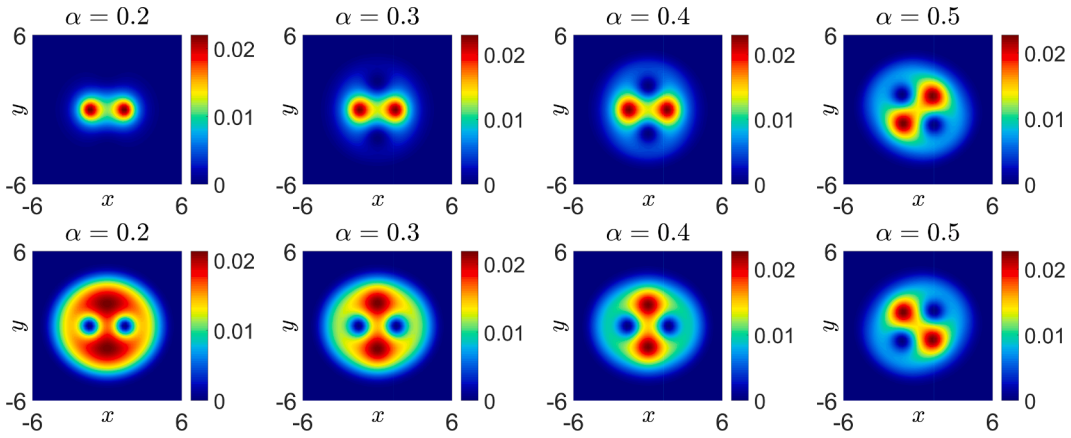

Fig. 1. Contour plots of the density $|\phi_\ell^g|^2$ with $\alpha = 0.2, 0.3, 0.4, 0.5$ (left to right) in Example 4.2.

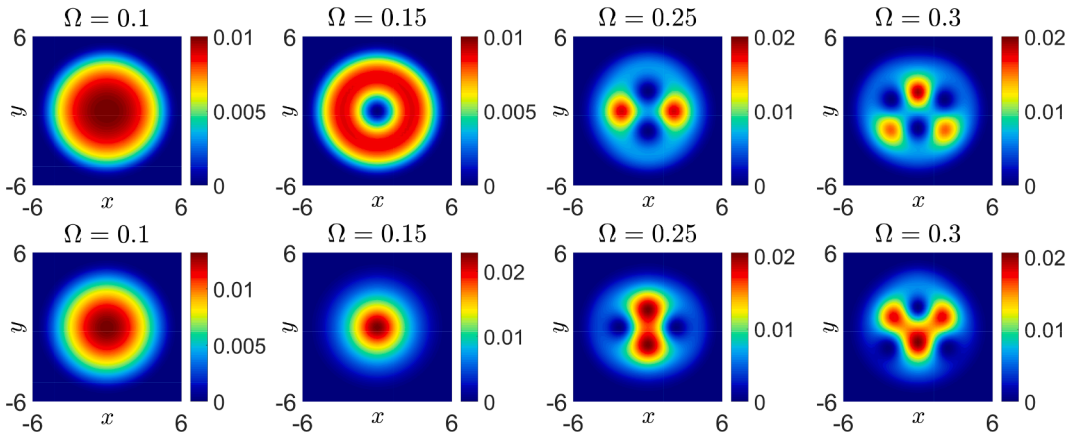

Fig. 2. Contour plots of the density $|\phi_\ell^g|^2$ with $\Omega = 0.1, 0.15, 0.25, 0.3$ (left to right) for **Case I** of Example 4.3.

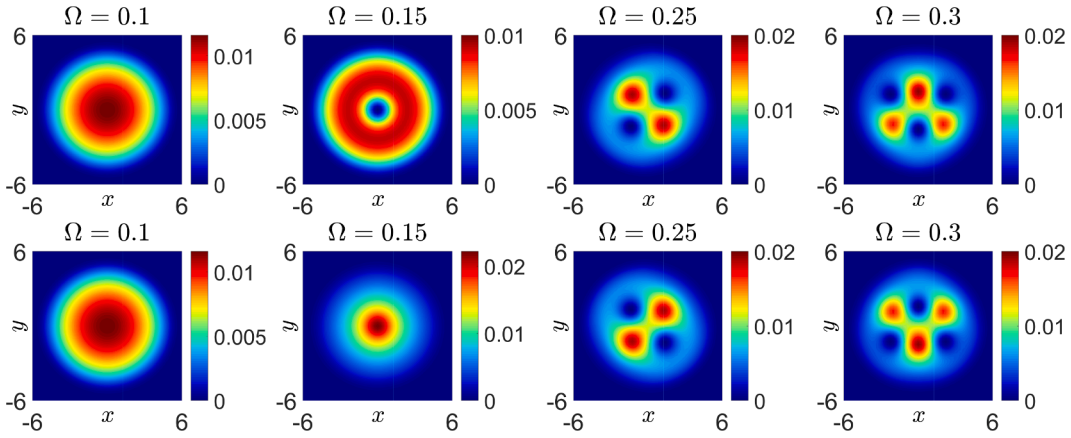

Fig. 3. Contour plots of the density $|\phi_\ell^g|^2$ with $\Omega = 0.1, 0.15, 0.25, 0.3$ (left to right) for **Case II** of Example 4.3.

Example 4.4 (Anisotropic potential)**.** In this example, we take anisotropic potential to investigate the vortex structures in ground states. To this end, we consider $V_1(\mathbf{x}) = V_2(\mathbf{x}) = \frac{1}{2}(\gamma_x^2 x^2 + y^2)$ and choose γ_x as $0.46, 0.5, 0.7$ respectively compared with $\gamma_x = 1$. We set $\Omega = 0.3,\ \alpha = 0.5,\ \beta_{11} = \beta_{22} = 500,\ \beta_{12} = 490,\ \lambda_{ij} = 100$, and the dipole axis $\boldsymbol{n} = (0, 1, 0)^\top$.

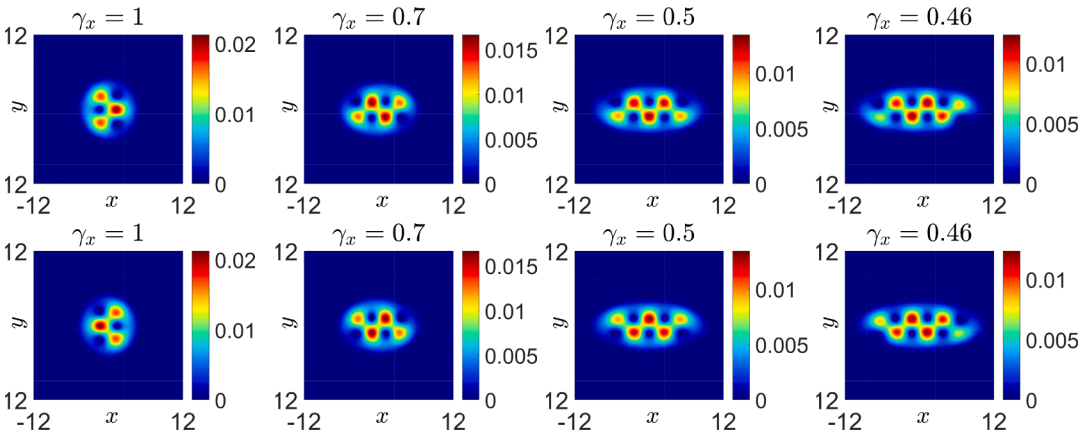

Fig. 4. Contour plots of the density $|\phi_\ell^g|^2$ with $\gamma_x = 1, 0.7, 0.5, 0.46$ (left to right) in Example 4.4.

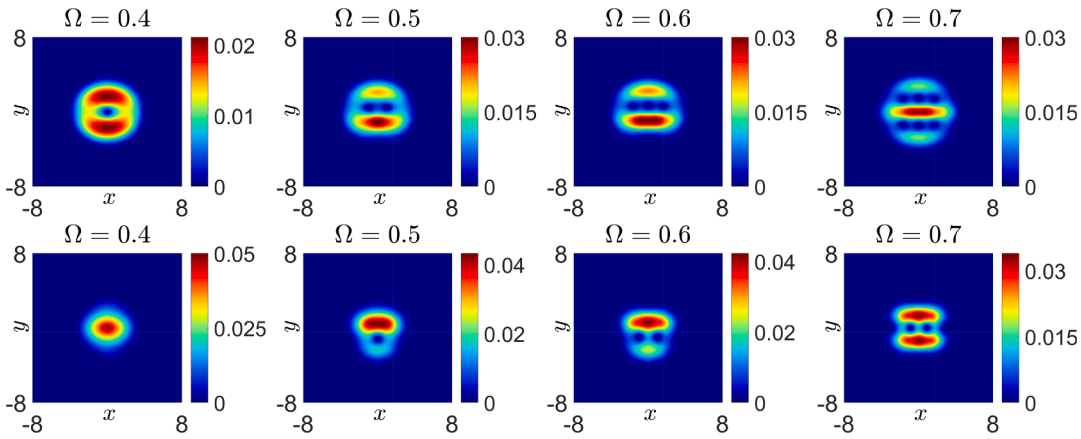

Fig. 5. Contour plots of the density $|\phi_\ell^g|^2$ with $\Omega = 0.4, 0.5, 0.6, 0.7$ (left to right) in Example 4.5.

Fig. 4 illustrates the contour plots of the density $|\phi_\ell^g|^2$ with different γ_x. From it, it is easy to see that as γ_x decreases, the density of each component extends further along the x-direction, showing stronger anisotropy strength, and also the vortex number of each component increases.

Example 4.5 (Stripe vortex structure)**.** In this example, we investigate the stripe pattern of the vortex structures in ground states for 2D case. To this end, we set $\alpha = 0.5,\ \beta_{11} = \beta_{12} = \beta_{22} = 110,\ \lambda_{11} = 99,\ \lambda_{12} = \lambda_{22} = 0$, and vary $\Omega = 0.4, 0.5, 0.6, 0.7$.

Fig. 5 shows the contour plots of the density $|\phi_\ell^g|^2$ with different Ω. From this picture, we observe that the vortices in one component localize within the density domains of the other component. These vortices align linearly, forming stripe-patterned density distributions consistent with the physical phenomena [42]. In addition, we can find that the numbers of vortices in both components (with and without DDI) increase with increasing angular velocity.

Example 4.6 (The ground states in 3D)**.** Here, we compute the ground states under different angular velocities in 3D. To this end, we take $\mathbf{R}_L = [-8, 8]^3,\ h = 1/8,\ \alpha = 0.5,\ \beta_{11} : \beta_{12} : \beta_{22} = (500 : 470 : 485),\ \lambda_{ij} = 100$, the dipole axis $\boldsymbol{n} = (0, 0, 1)^\top$, and $\Omega = 0.3, 0.45, 0.5, 0.6$.

Fig. 6 shows the isosurface $|\phi_\ell^g|^2 = 10^{-4}$ and the corresponding slice plots of $|\phi_\ell^g|^2$ perpendicular to rotation z-axis. From this figure, we can conclude that: (i) The vortex lines of each component extend towards the rotation z-axis generally. (ii) If there is only one vortex line in each component, the vortex line is not located in the center of the xy-plane. (iii) The number of vortex lines in each component increases as angular velocity rises.

Remark 4.1. For each example, we tried at least $10 \times 10 = 100$ combinations of initial guess to compute the ground states numerically. And we find that it is more likely to obtain the ground states by using different types of initial guess for the two components. In fact, for symmetric parameters, i.e., $\beta_{11} = \beta_{22},\ \lambda_{11} = \lambda_{22}, \alpha = 0.5$, the density of each component can interchange without affecting the energy.

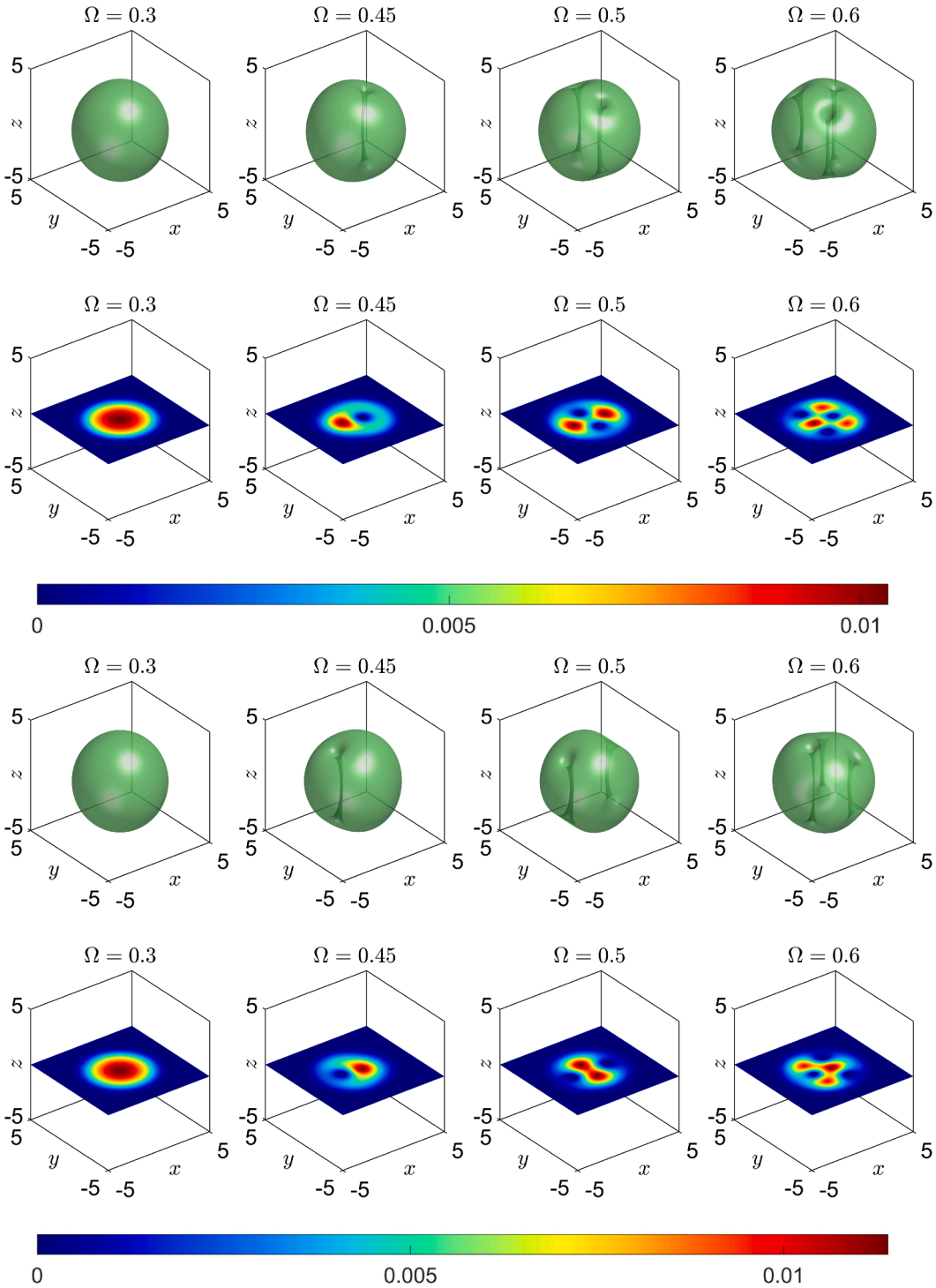

Fig. 6. Isosurface of $|\phi_\ell^g|^2 = 10^{-4}$ (the first and the third row respectively) and slice of $|\phi_\ell^g|^2$ perpendicular to the rotation z-axis (the second and the fourth row respectively) in Example 4.6.

5. Conclusion

In this paper, we studied the existence and uniqueness of the ground states of two-component dipolar BECs for both non-rotating and rotating cases. Then, to compute the ground states, we integrated the gradient flow with Lagrange multiplier (GFLM) method with the optimal kernel truncation method (KTM) for DDI evaluation, which is implemented purely by the discrete Fast Fourier Transform achieving nearly optimal efficiency. Our algorithm is spectrally accurate in space, efficient, and easy to implement. Lastly, we investigated the structure of ground states under different model parameters, including the mass distribution, short-range interaction strength, angular velocity, and anisotropic trapping potential. We present extensive numerical examples in both 2D and 3D to support our exploration. Indeed, our algorithm is easy to extend to other relevant problems and provides a powerful tool for investigating the ground state structures of multi-component rotating dipolar BECs.

CRediT authorship contribution statement

Wenlei Li: Writing – original draft, Resources, Methodology, Investigation, Formal analysis; **Qinglin Tang:** Writing – review & editing, Visualization, Supervision, Resources, Methodology, Formal analysis, Conceptualization; **Jing Wang:** Writing – review & editing, Writing – original draft, Resources, Methodology, Investigation, Formal analysis, Conceptualization; **Yong Zhang:** Writing – review & editing, Visualization, Validation, Supervision, Software, Resources, Project administration, Methodology, Investigation, Funding acquisition, Formal analysis, Data curation, Conceptualization; **Ruijie Zou:** Writing – review & editing, Writing – original draft, Visualization, Validation, Software, Methodology, Investigation, Formal analysis, Data curation.

Data availability

Data will be made available on request.

Declaration of competing interest

The authors declare the following financial interests/personal relationships which may be considered as potential competing interests:

Qinglin Tang reports financial support was provided by the National Natural Science Foundation of China. Qinglin Tang reports financial support was provided by the Natural Science Foundation of Sichuan Province. Qinglin Tang reports financial support was provided by the Institutional Research Fund from Sichuan University. Wenlei Li reports financial support was provided by the National Natural Science Foundation of China. Yong Zhang reports financial support was provided by the National Natural Science Foundation of China. Ruijie Zou reports financial support was provided by the National Natural Science Foundation of China. If there are other authors, they declare that they have no known competing financial interests or personal relationships that could have appeared to influence the work reported in this paper.

Acknowledgments

The authors thank Mr. Wei Yang and Mr. Zixu Feng for helpful suggestions and stimulating discussions. This work was partially supported by the National Natural Science Foundation of China Grant no. 11971335, the Natural Science Foundation of Sichuan Province Grant no. 2024NSFSC0438 and the Institutional Research Fund from Sichuan University Grant no. (Q. Tang), the National Natural Science Foundation of China Grant no. 12171197 (W. Li) and No. 12271400 (Y. Zhang and R. Zou).

References

[1] M.H. Anderson, J.R. Ensher, M.R. Matthews, C.E. Wieman, E.A. Cornell, Observation of Bose–Einstein condensation in a dilute atomic vapor, Science 269 (1995) 198–201.
[2] J.R. Abo-Shaeer, C. Raman, J.M. Vogels, W. Ketterle, Observation of vortex lattices in Bose–Einstein condensates, Science 292 (2001) 476–479.
[3] V. Bretin, S. Stock, Y. Seurin, J. Dalibard, Fast rotation of a Bose–Einstein condensate, Phys. Rev. Lett. 92 (2004) 50403.
[4] A. Griesmaier, J. Werner, S. Hensler, J. Stuhler, T. Pfau, Bose–Einstein condensation of chromium, Phys. Rev. Lett. 94 (2005) 160401.
[5] W. Bao, Y. Cai, Mathematical theory and numerical methods for Bose–Einstein condensation, Kinet. Relat. Mod. 6 (2013) 1–135.
[6] W. Bao, Y. Cai, H. Wang, Efficient numerical methods for computing ground states and dynamics of dipolar Bose–Einstein condensates, J. Comput. Phys. 229 (2010) 7874–7892.
[7] T.F. Jiang, W.C. Su, Ground state of the dipolar Bose–Einstein condensate, Phys. Rev. A 74 (2006) 63602.
[8] Y. Zhao, J. An, C. Gong, Vortex competition in a rotating two component dipolar Bose–Einstein condensate, Phys. Rev. A 87 (2013) 13605.
[9] W. Bao, N.B. Abdallah, Y. Cai, Gross–Pitaevskii–Poisson equations for dipolar Bose–Einstein condensate with anisotropic confinement, SIAM J. Math. Anal. 44 (2012) 1713–1741.
[10] Y. Cai, M. Rosenkranz, Z. Lei, W. Bao, Mean-field regime of trapped dipolar Bose–Einstein condensates in one and two dimensions, Phys. Rev. A 82 (2010) 043623.
[11] X. Antoine, C. Besse, R. Duboscq, V. Rispoli, Acceleration of the imaginary time method for spectrally computing the stationary states of Gross–Pitaevskii equations, Comput. Phys. Commun. 219 (2017) 70–78.
[12] H. Chen, G. Dong, W. Liu, Z. Xie, Second-order flows for computing the ground states of rotating Bose–Einstein condensates, J. Comput. Phys. 475 (2023) 111872.
[13] I. Danaila, P. Kazemi, A new Sobolev gradient method for direct minimization of the Gross–Pitaevskii energy with rotation, SIAM J. Sci. Comput. 32 (2010) 2447–2467.

[14] W. Liu, Y. Cai, Normalized gradient flow with Lagrange multiplier for computing ground states of Bose–Einstein condensates, SIAM J. Sci. Comput. 43 (2021) 219–B242.
[15] Q. Zhuang, J. Shen, Efficient SAV approach for imaginary time gradient flows with applications to one- and multicomponent Bose–Einstein condensates, J. Comput. Phys. 396 (2019) 72–88.
[16] X. Antoine, A. Levitt, Q. Tang, Efficient spectral computation of the stationary states of rotating Bose–Einstein condensates by preconditioned nonlinear conjugate gradient methods, J. Comput. Phys. 343 (2017) 92–109.
[17] X. Antoine, Q. Tang, Y. Zhang, A preconditioned conjugated gradient method for computing ground states of rotating dipolar Bose–Einstein condensates via kernel truncation method for dipole-dipole interaction evaluation, Commun. Comput. Phys. 24 (2018) 966–988.
[18] I. Danaila, B. Protas, Computation of ground states of the Gross–Pitaevskii functional via Riemannian optimization, SIAM J. Sci. Comput. 39 (2017) 1102–B1129.
[19] Q. Shu, Q. Tang, S. Zhang, Y. Zhang, A preconditioned Riemannian conjugate gradient method for computing the ground states of arbitrary-angle rotating Bose–Einstein condensates, J. Comput. Phys. 512 (2024) 113130.
[20] G. Vergez, I. Danaila, S. Auliac, F. Hecht, A finite-element toolbox for the stationary Gross–Pitaevskii equation with rotation, Comput. Phys. Commun. 209 (2016) 144–162.
[21] X. Wu, Z. Wen, W. Bao, A regularized Newton method for computing ground states of Bose–Einstein condensates, J. Sci. Comput. 73 (2017) 303–329.
[22] C.M. Dion, E. Cancès, Ground state of the time-independent Gross–Pitaevskii equation, Comput. Phys. Commun. 177 (2007) 787–798.
[23] Y. Wang, B. Jeng, C. Chien, A two-parameter continuation method for rotating two-component Bose–Einstein condensates in optical lattices, Commun. Comput. Phys. 13 (2013) 442–460.
[24] F. Xu, H. Xie, M. Xie, M. Yue, A multigrid method for the ground state solution of Bose–Einstein Condensates based on Newton iteration, 2021, pp. 645–663.
[25] P. Huang, Q. Yang, Newton-based alternating methods for the ground state of a class of multi-component Bose–Einstein condensates, SIAM J. Optim. 34 (3) (2024) 3136–3162.
[26] H. Wang, Numerical simulations on stationary states for rotating two-component Bose–Einstein condensates, J. Sci. Comput. 38 (2009) 149–163.
[27] Y. Zhang, Fast evaluation of convolution-type nonlocal potential, Math. Numer. Sin. 45 (4) (2023) 385–400.
[28] S. Jiang, L. Greengard, W. Bao, Fast and accurate evaluation of nonlocal Coulomb and dipole-dipole interactions via the nonuniform FFT, SIAM J. Sci. Comput. 36 (2014) 777–794.
[29] L. Exl, N.J. Mauser, Y. Zhang, Accurate and efficient computation of nonlocal potentials based on Gaussian-sum approximation, J. Comput. Phys. 327 (2016) 629–642.
[30] X. Liu, Q. Tang, S. Zhang, Y. Zhang, On optimal zero-padding of kernel truncation method, SIAM J. Sci. Comput. 46 (1) (2024) 23–A49.
[31] F. Vico, L. Greengard, M. Ferrando, Fast convolution with free-space Green's functions, J. Comput. Phys. 323 (2016) 191–203.
[32] L. Greengard, S. Jiang, Y. Zhang, The anisotropic truncated kernel method for convolution with free-space Green's functions, SIAM J. Sci. Comput. 40 (6) (2018) 3733–A3754.
[33] E.H. Lieb, R. Seiringer, J. Yngvason, Bosons in a trap: a rigorous derivation of the Gross–Pitaevskii energy functional, Phys. Rev. A, 61 (2000), 043602.
[34] M. Reed, B. Simon, Methods of Modern Mathematical Physics IV: Analysis of Operators, Elsevier, 1978.
[35] W. Bao, H. Wang, P.A. Markowich, Ground, symmetric and central vortex states in rotating Bose–Einstein condensates, Commun. Math. Sci. 3 (2005) 57–88.
[36] Z. Li, Q. Tang, H. Wang, Y. Zhang, Numerical studies on ground state of dipolar spin $F = 1$ Bose–Einstein condensate, In preparation.
[37] A. Dutt, V. Rokhlin, Fast Fourier transforms for nonequispaced data, SIAM J. Sci. Comput. 14 (1993) 1368–1393.
[38] L. Greengard, J.Y. Lee, Accelerating the nonuniform fast Fourier transform, SIAM Rev. 46 (2004) 443–454.
[39] W. Bao, Q. Tang, Y. Zhang, Accurate and efficient numerical methods for computing ground states and dynamics of dipolar Bose–Einstein condensates via the nonuniform FFT, Commun. Comput. Phys. 19 (5) (2016) 1141–1166.
[40] W. Bao, Q. Du, Computing the ground state solution of Bose–Einstein condensates by a normalized gradient flow, SIAM J. Sci. Comput. 25 (2004) 1674–1697.
[41] W. Bao, I.-L. Chern, F.Y. Lim, Efficient and spectrally accurate numerical methods for computing ground and first excited states in Bose–Einstein condensates, J. Comput. Phys. 219 (2006) 836–854.
[42] X. Zhang, L. Wen, C. Dai, R. Dong, H. Jiang, H. Chang, S. Zhang, Exotic vortex lattices in a rotating binary dipolar Bose–Einstein condensate, Sci. Rep. 6 (1) (2016) 19380.